



# An MHD Simulation of Solar Active Region 11158 Driven with a Time-dependent Electric Field Determined from HMI Vector Magnetic Field Measurement Data

Keiji Hayashi<sup>1,2</sup> , Xueshang Feng<sup>1,3</sup> , Ming Xiong<sup>1,3</sup> , and Chaowei Jiang<sup>3</sup>

<sup>1</sup> SIGMA Weather Group, State Key Laboratory for Space Weather, National Space Science Center, Chinese Academy of Sciences, Beijing 100190, People's Republic of China; [keiji@Sun.stanford.edu](mailto:keiji@Sun.stanford.edu), [fengx@spaceweather.ac.cn](mailto:fengx@spaceweather.ac.cn), [mxiong@swl.ac.cn](mailto:mxiong@swl.ac.cn)

<sup>2</sup> Institute of Space-Earth Environmental Research, Nagoya University, Nagoya, Aichi, 464-8601, Japan

<sup>3</sup> Institute of Space Science and Applied Technology, Harbin Institute of Technology, Shenzhen, 518055, People's Republic of China; [chaowei@hit.edu.cn](mailto:chaowei@hit.edu.cn)

Received 2017 October 30; revised 2018 January 31; accepted 2018 January 31; published 2018 February 28

## Abstract

For realistic magnetohydrodynamics (MHD) simulation of the solar active region (AR), two types of capabilities are required. The first is the capability to calculate the bottom-boundary electric field vector, with which the observed magnetic field can be reconstructed through the induction equation. The second is a proper boundary treatment to limit the size of the sub-Alfvénic simulation region. We developed (1) a practical inversion method to yield the solar-surface electric field vector from the temporal evolution of the three components of magnetic field data maps, and (2) a characteristic-based free boundary treatment for the top and side sub-Alfvénic boundary surfaces. We simulate the temporal evolution of AR 11158 over 16 hr for testing, using *Solar Dynamics Observatory*/Helioseismic and Magnetic Imager vector magnetic field observation data and our time-dependent three-dimensional MHD simulation with these two features. Despite several assumptions in calculating the electric field and compromises for mitigating computational difficulties at the very low beta regime, several features of the AR were reasonably retrieved, such as twisting field structures, energy accumulation comparable to an X-class flare, and sudden changes at the time of the X-flare. The present MHD model can be a first step toward more realistic modeling of AR in the future.

**Key words:** magnetohydrodynamics (MHD) – Sun: magnetic fields – sunspots

## 1. Introduction

The structures of a magnetic field and their evolution above the solar surface are the consequences of the solar-surface magnetic field and plasma motions varying continuously in time. On a global scale, coronal streamers and coronal holes are evidence of gradual long-term evolution on the solar photosphere, such as the poleward migration of magnetic flux, solar differential rotation, and meridional circulation. On a small scale, the dynamics of the solar active region (AR) is primarily controlled by the emergence, development, and complex motions of strong magnetic field polarity pair(s). Typically, the timescale of the solar-surface magnetic field evolution is much shorter than the magnetic relaxation time (i.e., dissipation): therefore, the evolution of the photospheric magnetic field results in non-potential magnetic field structures above the photosphere that can be a cradle of energy build-up processes. The magnetic free energy, often at the compact central regions of the AR system, can be suddenly released through, probably, a rapid magnetic reconnection process, to accelerate and/or heat the plasma, which is observed as a solar flare (e.g., Schrijver 2016).

To better understand the dynamics in an AR system, it is desirable to have observation-based three-dimensional descriptions and depictions of the magnetic field and plasma there. In general, however, direct measurements of the AR magnetic field above the solar photosphere are limited because of the signals from the target volumes are weaker than the (noise) signals from the photosphere. Several modeling approaches have been developed to determine the three-dimensional structure from photospheric conditions that can be much more accurately measured (see Guo et al. 2017 and references therein).

One approach is to apply the vacuum-limit assumption, which reasonably represents the very low- $\beta$  situation in the solar corona ( $\beta = P_g/(B^2/8\pi)$ ). Under the vacuum-limit assumption, several models, such as the potential field (PF) model (Schmidt 1964; Altschuler & Newkirk 1969; Schatten et al. 1969; Sakurai 1982), linear force-free field model (Nakagawa et al. 1971; Nakagawa & Raadu 1972), nonlinear force-free field (NLFFF) model (e.g., Sakurai 1981; Regnier & Canfield 2006; Wiegmann et al. 2006, 2012; Bobra et al. 2008), and non-force-free field (NFFF) model (e.g., Hu & Dasgupta 2008; Duan et al. 2017), have been developed. In many cases, these models can directly use data from the photospheric magnetic field observation as boundary values, which allows one to set up a realistic situation at an instant and/or region of interest. In many studies using these vacuum-limit models, the temporal variation of the modeled system can be traced by calculating time-series solutions of a static extrapolation, each of which is independent. Hence, the variations obtained by these vacuum-limit models are, although overall quite reasonable, not exactly the temporal evolution of the nonlinear sub-Alfvénic system, where a state at a certain instant is affected by states in earlier times.

Another more physics-based but computationally expensive approach is to apply a time-dependent magnetohydrodynamics (MHD) simulation. The MHD model approach (cf., Janvier et al. 2015 and references therein) is probably the only strategy to assess straightforwardly the interaction between the plasma and magnetic field in the sub-Alfvénic region, and hence their temporal evolution in the AR system.

There are two types of the so-called MHD models. In the first type, the plasma density and temperature are taken into account but are not solved explicitly (for example, by assuming they are constant and/or proportional to the local field

strength). Omitting the plasma from the governing equation system is allowed when studying the solar AR, where the  $\beta$  ratio is very low. This type of modeling, typically through relaxation schemes, can obtain solutions for magnetic field structures that satisfy the Lorentz-force-free and divergence-free conditions (e.g., Inoue et al. 2012; Jiang et al. 2013b; Zhu et al. 2013) to examine the structure of a highly nonlinear state of AR magnetism and the stability of the magnetic system and to trace its temporal evolution (e.g., Cheung & DeRosa 2012; Guo et al. 2012; Gibb et al. 2014; Inoue et al. 2014; Jiang et al. 2014; Yeates 2014).

The other type of MHD model fully solves the MHD equations, including the plasma quantities, explicitly. Being capable of handling magnetosonic waves and including gravity, the full- and time-dependent MHD model can be the best choice for examining the dynamics of a sub-Alfvénic AR system responding to time-evolving solar-surface boundary conditions. There have been several successful efforts using full three-dimensional time-dependent MHD simulation models (e.g., Wu et al. 2006, 2012; Aulanier et al. 2010; Fan et al. 2011; Yang et al. 2012; Jiang & Feng 2013; Jiang et al. 2013a; Galsgaard et al. 2015) that can reproduce several magnetic features in the AR system as observed. This full MHD method can also reproduce the surrounding magnetic field structures around the AR, which are believed to be an important factor in determining whether or not the twisted system in the core of the AR system will erupt (e.g., Liu & Hayashi 2006; Liu 2008; Joshi et al. 2014). Coupled with the heating mechanism, we can also produce detailed structures of the plasma quantities (e.g., Mok et al. 2005; Bourdin et al. 2013). Recently, Jiang et al. (2016) successfully simulated the entire life cycle of an AR, from magnetic flux emergence and formation to the eruption of a twisted magnetic loop. The temporally evolving boundary conditions of the magnetic field can be applied to MHD simulations of the global corona (e.g., Feng et al. 2012; Hayashi 2013), interplanetary space (e.g., Hayashi 2012; Shiota & Kataoka 2016), and both corona and interplanetary space (e.g., Feng et al. 2015, 2017), too. These data-driven MHD models with a time-dependent observation-based boundary magnetic field distribution can provide us with detailed, physics- and observation-based three-dimensional descriptions of the dynamics in the solar corona and solar wind as a result of photospheric variations (e.g., Harra et al. 2012).

For data-driven MHD simulations of the AR, one has to first choose and calculate the boundary driving parameter(s) from observations. Among several choices allowed, the following three choices are commonly selected. The first choice is to give the observation-based magnetic field data directly as the boundary values. The second one is to determine the plasma flow and to drive the simulated magnetic field through the induction equation,  $\partial_t \mathbf{B} = \nabla \times (\mathbf{V} \times \mathbf{B})$ . The third choice is to determine the electric field ( $\mathbf{E}$ ) and to drive the magnetic field as  $\partial_t \mathbf{B} = -\nabla \times \mathbf{E}$ .

The motions of the plasma and magnetic field on the photosphere play critically important roles in the energy supply throughout the photosphere (e.g., Leka et al. 1996; Kusano 2002; Demoulin & Berger 2003; Kusano et al. 2004). In all probability, Levine & Nakagawa (1974) were the first to try to determine photospheric plasma motions from time series of the photospheric magnetic field and through the induction equation. Since then, several sophisticated algorithms have

been developed (see Welsh et al. 2007 and references therein), for example, the methods using local correlation tracking (LCT; e.g., Choe et al. 2001; Moon et al. 2002), the minimum-energy method (Longcope 2004), the inductive LCT method (ILCT; Welsh et al. 2004), and DAVE4VM (the differential affine velocity estimator for vector magnetograms; Schuck 2006, 2008). The simulation driven with the solar-surface plasma motions is, in this way, very attractive. However, the difference between the observed solar-surface magnetic field and the simulated one can grow substantially in the case of long-time simulation runs, at least in our provisional runs with our MHD model.

The electric field as a boundary driving parameter can allow us to reproduce exactly the evolution of the observed magnetic field on the (solar-surface) boundary, within minor numerical errors (i.e., Fisher et al. 2010, 2012; Kazachenko et al. 2014; Lumme et al. 2017). Because of the lack of information on the vertical gradients of the magnetic field on and around the solar photosphere, however, we need to make assumption(s) to complete the equation system. In addition, the calculation algorithm can often be complicated. Therefore, a simple calculation algorithm capable of reproducing the observed evolution of the magnetic field is desirable.

In the MHD simulations for the AR, we usually have to limit the sub-Alfvénic simulation region to limit the needed computational resources to a reasonable amount. The simulation region is a cubic box with the bottom boundary accommodating the observation-based quantities as the boundary values, and the top and side boundary surfaces are set. The periodic boundary condition in the horizontal directions can be a good choice; however, this choice often results in unreasonably distorted structures of the simulated magnetic field and plasma. Therefore, the proper treatment of the sub-Alfvénic free boundary condition is a must. The projected normal characteristics method (e.g., Nakagawa & Steinolfson 1976; Nakagawa et al. 1987; Wu & Wang 1987) is a simplified version of the characteristic-based boundary treatment and can treat sub-Alfvénic boundary surfaces, including the free boundary surfaces (on which observation-based constraints cannot be imposed).

As part of our effort to develop the data-driven MHD model for the AR, we established a time-dependent three-dimensional MHD model with two features: the simulated variables are driven with a bottom-boundary electric field, and the sub-Alfvénic boundary surfaces are treated with the projected normal characteristics method.

As required for calculating the solar-surface electric field, the input solar-surface vector magnetic field should have a sufficiently short cadence and high spatial resolution to trace magnetic features on the solar photosphere. The Helioseismic Magnetic Imager (HMI) on board the *Solar Dynamics Observatory* (SDO) satellite (Scherrer et al. 2012; Schou et al. 2012) has been observing the full disk of the Sun, with about a 1 arcsec angular resolution and 45 s cadence for the magnetogram and 12 minutes or 135 s for the vector magnetic field, almost nonstop since 2010 May 1. With its cadence and spatial resolution ( $\sim 350$  km near the center of solar disk), the HMI data can offer the desired vector magnetic field data for tracing photospheric motions with apparent speeds of less than  $0.5 \text{ km s}^{-1}$  (in 720 s cadence observation data). As also theoretically examined in Leake et al. (2017), therefore, this cadence is short enough for most solar photospheric phenomena (a few exceptions can be pointed out, such as the emergence of

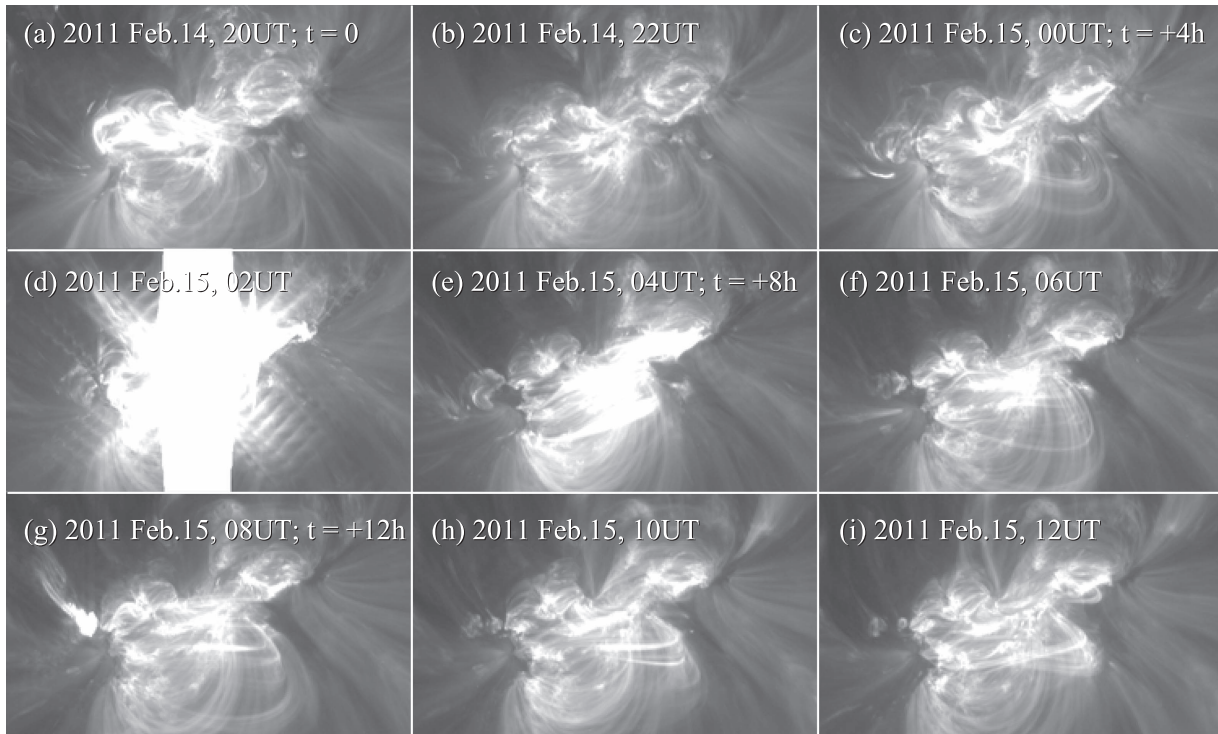


**Figure 1.** AIA 193 Å images taken every two hours starting on (a) 2011 February 14, 20:00 UT until (i) 2011 February 15, 12:00 UT. The X-class flare started around 01:44 UT on February 15 and reached the X-ray intensity peak around 1:56 UT.

horizontally elongated magnetic flux whose photospheric cross-section can appear as a feature that is often moving faster than the local photospheric sound speed).

As a case study, we choose the AR NOAA 11158 and selected a 16 hr span of time from 2011 February 14 20:00 UT to February 15, 12:00 UT. This region was remarkably very active, producing an X-class flare that started around 01:44 with its X-ray intensity peak at 01:56 UT on 2011 February 15. Many M- and C-class flares followed. This X-class flare region has been widely analyzed and simulated (e.g., Jing et al. 2012; Sun et al. 2012; Wang et al. 2012; Zhao et al. 2014). Figure 1 shows the *SDO*/AIA 193 Å images (Lemen et al. 2012), taken over the 16 hr span.

This paper is organized as follows. In Section 2, we briefly describe the HMI vector magnetic field data used in this study. In Section 3, the method for calculating the electric field usable in a data-driven MHD simulation is described. The difference equations for retrieving the temporal variations of the magnetic field vector on the bottom boundary are given in Appendix A. In Section 4, the framework of the present model, a time-dependent three-dimensional compressive MHD simulation model, and the treatments for the top and side boundary surfaces are described. Appendix B details the characteristics-based treatments for the sub-Alfvénic top and side free boundary surfaces. In Section 5, the simulation results are presented. The discussion and summary are given in Section 6.

## 2. Observation Data: HMI Vector Magnetic Field Data

From the HMI measurements at the 6173 Å Fe I line, three-component vector magnetic field data are regularly produced at the Joint Science Operations Center (JSOC) data pipeline. The data products are available at the HMI/JSOC database (<http://jsoc.stanford.edu/ajax/lookdata.html>). In the data

process, the VFISV (Very Fast Inversion for Stokes Vector; Borrero et al. 2011) is applied to calculate the parameters of the magnetized solar atmosphere, such as the strength, inclination, and azimuth angles of the magnetic field, line depth and width, and line-of-sight Doppler velocity (Centeno et al. 2014). Then, the 180° ambiguity in the azimuth angle is solved by means of the minimum-energy algorithm (Metcalf 1994; Leka et al. 2009) to finally yield three components of the magnetic field over the solar disk. The HARP (HMI Active Region Patch; M. Turmon et al. 2017, in preparation) module can automatically recognize magnetically active regions, and the SHARP (Space weather HARP; Bobra et al. 2014) module calculates various space-weather indices, such as surface integrations of current helicity, and other non-potentiality indices, such as the Lorentz force, within the AR recognized by the HARP module. Details of the HMI vector magnetic field data products and processes are given in Hoeksema et al. (2014).

The SHARP CEA (cylindrical equi-area) data sets, which are a subset of the SHARP products, are constructed in the local spherical coordinate frame moving with solar differential rotation. We used the data set identified as `hmi.SHARP_720s_CEA[377][ ]` at the JSOC database with the internal serial number 377 for AR 11158. Three segments (subsets) of this data set,  $B_r$ ,  $B_\theta$ , and  $B_\phi$ , which represent the radial ( $B_r$ ), latitudinal ( $B_\theta$ ), and longitudinal ( $B_\phi$ ) components, respectively, are used. In this study, we use a simple conversion from local spherical coordinates to the Cartesian coordinates:  $B_x(=B_\phi)$ ,  $B_y(=-B_\theta)$ , and  $B_z(=B_r)$ .

We use a series of 81 data maps of the 12 minute cadence observation data that cover in total a 16 hr period starting from 2011 February 14, 20:00 UT. Figure 2 demonstrates the vector magnetic field data at the first instant of this period. During this selected period, an X-class flare occurred around February 15,



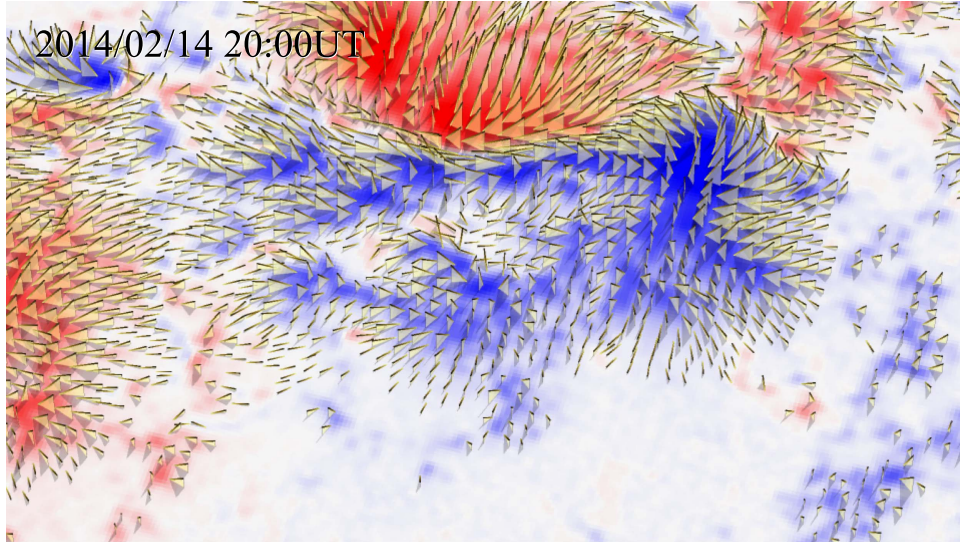


**Figure 2.** Demonstration of the HMI vector magnetogram data around the primary PIL, at the first instant of the selected 16 hr period (2014 February 14, 20:00 UT). The blue (red) color on the surface represents the positive (negative) polarity, and the colors are given proportional to the square root of  $B_z$ , so that the colors at weak field values are enhanced. The direction and length of the brown lines, which start from the data points with  $|B| \geq 300$  G or  $300 \text{ Mx cm}^{-2}$ , indicate the direction and strength of the surface field, respectively. Each brown line is attached to a transparent yellow triangle that is perpendicular to the bottom surface to enhance the three-dimensional sense for viewers.

01:47 UT ( $t = +5.78$  hr), near the central meridian viewed from the Earth. The original dimensions of the SHARP CEA data maps are 744 and 377 for the longitudinal direction (or the  $x$ -direction) and the latitudinal direction (or the  $y$ -direction), respectively. In order to reduce the required computational resources, we smoothed the maps spatially with the Gaussian function with a half width of six-pixel size (approximately 2900 km) and reduced the pixel number by 94 to 186 (1440 km per pixel) with boxcar averaging.

### 3. Electric Field on the Bottom-boundary Surface

Because we do not have a sufficient amount of information, particularly on the vertical gradients of the magnetic field around the photosphere, assumptions have to be made to complete the equation system. Among the possible choices allowed, the poloidal-toroidal decomposition method (i.e., Fisher et al. 2010) is probably the most promising method for this purpose. A set of convenient presentations of the poloidal-toroidal decomposition of the magnetic field variations and the associated electric field is provided in Fisher et al. (2012).

In data-driven simulations, one does not have to determine the electric field on a certain plane (i.e., the bottom-boundary surface). Instead, we want to assign the electric field vector at different heights, that is, at the bottom-boundary reference height (at  $z = 0$ ) and at the top and bottom cell face centers (at  $z = \pm \Delta z/2$ ), in such a way that the derived vector quantity can be straightforwardly introduced through the spatial differencing method. Indeed, this computational practice allows for a simple method, described below.

Any arbitrary vector  $\mathbf{b}$  given on the  $x$ - $y$  plane can be split into three parts,

$$\mathbf{b} = \mathbf{b}_z + \mathbf{b}_h = \mathbf{b}_z + \mathbf{b}_{h,\text{df}} + \mathbf{b}_{h,\text{cf}}, \quad (1)$$

where  $\mathbf{b}_z$  is the component normal to the plane ( $b_z \hat{\mathbf{z}}$ ), and  $\mathbf{b}_h$  is the rest horizontal component (parallel to the plane). The horizontal vector  $\mathbf{b}_h$  can be further decomposed into the divergence-free component (df) and curl-free component (cf).

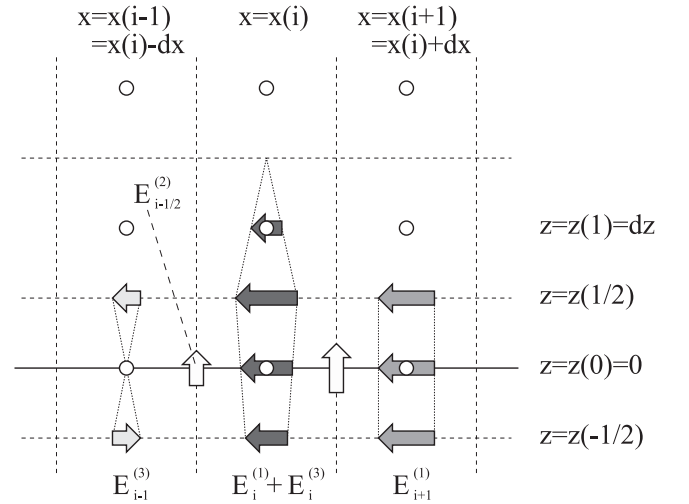


**Figure 3.** Positions of the electric field and the other vectors assigned in the discretized simulation grid system. The first part,  $\mathbf{E}^{(1)}$ , is calculated at the position of the cell center and is used to update  $B_z$  on the surface and at the first grid above it. The second part is assigned to the horizontal interface between the grids on the bottom boundary and used to update  $B_x$  and  $B_y$  on the bottom-boundary surface. The third part is at the cell interfaces with the neighboring grids in the vertical direction, and used to update  $B_x$  and  $B_y$  on the bottom boundary, and all three components at the grids above next to the bottom boundary.

Here, we seek the solutions of three vectors,  $\mathbf{E}^{(1)}$ ,  $\mathbf{E}^{(2)}$ , and  $\mathbf{E}^{(3)}$ , that satisfy

$$\begin{aligned} \nabla \times \mathbf{E}^{(1)} &= -\mathbf{B}'_z, & \nabla \times \mathbf{E}^{(2)} &= -\mathbf{B}'_{h,\text{df}} \\ \text{and } \nabla \times \mathbf{E}^{(3)} &= -\mathbf{B}'_{h,\text{cf}}, \end{aligned} \quad (2)$$

where the variables with a prime ( $'$ ) refer to the time derivatives of the observed magnetic field:  $B'_z (= \partial_t B_z)$ ,  $\mathbf{B}'_{h,\text{df}} (= \partial_t \mathbf{B}_{h,\text{df}})$ , and  $\mathbf{B}'_{h,\text{cf}} (= \partial_t \mathbf{B}_{h,\text{cf}})$ . Figure 3 shows the position assignment of these three parts of the electric field in discretized space. It should be noted here that the positions could be somewhat arbitrarily selected: our cell-centered simulation code uses the

electric field vectors, assigned or interpolated, at the center of the cell face or edge. The vector potential expression for the magnetic field may prefer the vectors at the edges and/or vertices.

The first part of the electric field,  $\mathbf{E}^{(1)}$ , has only two horizontal components. The vertical component of its curl matches the temporal variation of the vertical component of the magnetic field,

$$\hat{\mathbf{z}} \cdot (\nabla \times \mathbf{E}^{(1)}) = -B'_z. \quad (3)$$

For simplicity, its vertical gradient is assumed to be zero,

$$\frac{\partial \mathbf{E}^{(1)}}{\partial z} = 0. \quad (4)$$

This component can be calculated as

$$\mathbf{E}^{(1)} = \hat{\mathbf{z}} \times \nabla \Psi^{(1)}, \quad (5)$$

where  $\Psi^{(1)}$  is a scalar solution of a two-dimensional Poisson equation,

$$\nabla_h^2 \Psi^{(1)} + B'_z = 0. \quad (6)$$

The second part  $\mathbf{E}^{(2)}$  only has a vertical component and is placed at the center of the horizontal interface between the boundary numerical grid cells. Its curl matches the temporal evolution of the horizontal divergence-free component of the horizontal components of the magnetic field,

$$\nabla \times \mathbf{E}^{(2)} = -\mathbf{B}'_{h,df}. \quad (7)$$

The electric field is given as

$$\mathbf{E}^{(2)} = -\hat{\mathbf{z}} \Psi^{(2)}, \quad (8)$$

where  $\Psi^{(2)}$  is a scalar solution of the Poisson equation,

$$\begin{aligned} \nabla_h^2 \Psi^{(2)} + \hat{\mathbf{z}} \cdot (\nabla_h \times \mathbf{B}'_h) &= 0, \\ \text{hence } \nabla_h^2 \Psi^{(2)} + \hat{\mathbf{z}} \cdot (\nabla_h \times \mathbf{B}'_{h,df}) &= 0. \end{aligned} \quad (9)$$

The expressions for the first two electric field vectors,  $\mathbf{E}^{(1)}$  and  $\mathbf{E}^{(2)}$ , are basically the same as or very similar to those in Fisher et al. (2010, 2012).

To determine the third remaining part,  $\mathbf{E}^{(3)}$ , we assume that the divergence of the horizontal components of the magnetic field is straightforwardly related to the vertical gradient of the vertical component of the magnetic field through the divergence-free condition ( $\nabla \cdot \mathbf{B} = 0$ ),

$$\begin{aligned} \frac{\partial B_z}{\partial z} &= -\nabla_h \cdot \mathbf{B}_h, \quad \text{hence } \frac{\partial}{\partial z} \frac{\partial B_z^{(3)}}{\partial t} = -\nabla_h \cdot \mathbf{B}'_h \\ \text{or } \frac{\partial}{\partial z} \frac{\partial B_z^{(3)}}{\partial t} &= -\nabla_h \cdot \mathbf{B}'_{h,cf}. \end{aligned} \quad (10)$$

Because the observed temporal evolution of  $B_z$  is completely reproduced by only the first part ( $\mathbf{E}^{(1)}$ ), we want the contribution of the third part at the height of the bottom-boundary surface ( $z = 0$ ) to be zero. These two constraints can be satisfied when we define the additional temporal evolution

of the simulated  $B_z$  on the upper and lower faces as

$$\begin{aligned} \frac{\Delta B_z^{(3)}}{\Delta t} \bigg|_{z=(1/2)\Delta z} &= -\frac{\Delta B_z^{(3)}}{\Delta t} \bigg|_{z=-(1/2)\Delta z} \\ &= -\frac{1}{2} \Delta z \nabla_h \cdot \mathbf{B}'_{h,cf}, \end{aligned} \quad (11)$$

where  $\Delta z$  and  $\Delta t$  are the vertical size of the numerical cell and the observation data cadence (720 s in this study), respectively. Notice that this formula is equivalent to assuming that the diverging (converging) temporal evolution of the horizontal magnetic field components through the side boundary surfaces will be balanced by the vertical one converging (diverging) through the upper and bottom numerical cell faces evenly. Under this assumption, the third part of the electric field at the height  $z = +\Delta z/2$  is given as, in a manner similar to that for the first part,

$$\mathbf{E}^{(3)}|_{z=+\Delta z/2} = \hat{\mathbf{z}} \times \nabla_h \Psi^{(3)}, \quad (12)$$

with the scalar solution of the Poisson equation,

$$\begin{aligned} \nabla_h^2 \Psi^{(3)} - \frac{\Delta z}{2} \nabla_h \cdot \mathbf{B}'_h &= 0 \quad \text{or} \quad \nabla_h^2 \Psi^{(3)} - \frac{\Delta z}{2} \nabla_h \\ &\quad \cdot \mathbf{B}'_{h,cf} = 0. \end{aligned} \quad (13)$$

The electric field at the height  $z = -\Delta z/2$  is given as

$$\mathbf{E}^{(3)}|_{z=-\Delta z/2} = -\mathbf{E}^{(3)}|_{z=+\Delta z/2}. \quad (14)$$

We use an iterative differencing method to solve the three Poisson equations, in which the equation  $\partial_\tau \Psi = \nabla_h^2 \Psi + S$  ( $S$  is a source term and  $\tau$  is non-physical pseudo-time) is solved until the scalar solution sufficiently converges.

The vertical component of the magnetic field,  $B_z$ , at the  $(n+1)$ th time step is calculated through a curl on the  $x$ - $y$  plane,

$$B_z^{n+1} = B_z^n - (\nabla_h \times \mathbf{E}^{(1)}) \Delta t, \quad (15)$$

and the evolution of the horizontal components,  $B_x$  and  $B_y$ , are given through curls of the electric field vectors on the  $y$ - $z$  and  $z$ - $x$  plane, respectively,

$$\mathbf{B}_h^{n+1} = \mathbf{B}_h^n - \nabla \times (\mathbf{E}^{(2)} + \mathbf{E}^{(3)}) \Delta t. \quad (16)$$

In Appendix A, it is shown that the curl operations for the three electric field vector parts yield the target temporal evolution of the magnetic field. It should be mentioned that the three electric field vectors are designed to be used together: for example, one may want to use only the first part when only  $B_z$  data are available; however, only  $B_z$  is driven with the curl of  $\mathbf{E}^{(1)}$  whose horizontal components are assumed to be zero ( $\partial_z \mathbf{E}^{(1)} = 0$ ). To drive the other two horizontal components in a physically consistent manner, one has to remove the assumption of zero vertical gradient and construct difference equations of the curl of  $\mathbf{E}^{(1)}$  accordingly.

To preserve the divergence-free condition, the temporal variation of the magnetic field at the height  $z = 1 \cdot \Delta z$  (next to the bottom boundary) are calculated by summing contributions from both the simulated MHD variables (that is,  $\mathbf{V}$  and  $\mathbf{B}$ ) and the driving electric field given at the height  $z = +(1/2)\Delta z$  (given in Equations (5) and (14)). The energy density,  $\mathcal{E}$ , is adjusted in accordance with the difference of the square of the

magnetic field strength updated with and without additional electric field vectors at  $z = +(1/2)\Delta z$ .

Ideally, the electric field estimation should not include any parameters that are given for computational reasons. In our estimation, however, the third part of the electric field ( $\mathbf{E}^{(3)}$ ) has a parameter  $\Delta z$  that is not physics based or observation based. This came from an implicit, and inevitable, at least in this study, assumption that the horizontal components of the magnetic field  $\mathbf{B}_h$  and its temporal variation are uniform in the vertical direction (or their vertical gradients are zero) within the vertical numerical grid size. Unless additional constraint(s) on the gradient are given from observations and/or theoretical approaches, this assumption is inevitable.

Figure 4 shows scatter plots of the three components of the observed and reproduced magnetic field at several instants to demonstrate how well the derived electric field vector can reproduce the observed temporal evolution of the boundary magnetic field. Overall good agreements between the reproduced values and observations are found. Except for  $B_x$  and  $B_y$  at  $t = 0$ , the correlation coefficients are about 0.99, with very small offsets. Small displacements from the diagonal are due to the errors in spatial differencing in the iterative Poisson solver in the bounded domain. Cleaning the divergence of  $\mathbf{B}$  and the errors in estimating the third part (Equation (31)) contributes to the scatter in the horizontal components to some extent. The magnitude of the cumulative errors is reasonably small even at the 75th frame of the data map (at  $t = +15$  hr), in spite of the fact that the error is essentially accumulative with respect to time. Hence, we can conclude that the methodology is appropriate.

The plots in Figure 5 show the simulated  $B_z$  maps at  $t = 0$  and  $t = +15$  hr around the center of the bottom-boundary surface. Several features of the observed evolution, highlighted with a yellow circle and horizontal line, are indeed reproduced. The middle row in Figure 6 shows the distribution of the differences in the three components of the reproduced and observed magnetic field vectors at  $t = +15$  hr. Differences of noticeably large magnitude are found at strong-field regions, although overall the disagreements are relatively small: the 99th percentile of the ratio of the absolute difference to the absolute value of observation data at  $|B| > 200$  G was 0.07, which is reasonably acceptable. The magnitude of the disagreements can probably be reduced further if the staggered grid system is properly applied in the iterative Poisson solver.

## 4. Model Framework

### 4.1. Time-dependent MHD Simulation

The governing equations are the ideal compressive MHD equations under the gravity of the Sun,

$$\frac{\partial \varrho}{\partial t} = -\nabla \cdot (\varrho \mathbf{V}), \quad (17)$$

$$\begin{aligned} \frac{\partial(\varrho \mathbf{V})}{\partial t} = & -\nabla \cdot \left( P_g + \varrho \mathbf{V} : \mathbf{V} - \frac{1}{4\pi} \mathbf{B} : \mathbf{B} + \frac{B^2}{8\pi} \right) \\ & - \varrho \mathbf{g} - (\nabla \cdot \mathbf{B}) \mathbf{B}, \end{aligned} \quad (18)$$

$$\frac{\partial \mathbf{B}}{\partial t} = -\nabla \cdot (\mathbf{V} : \mathbf{B} - \mathbf{B} : \mathbf{V}) - (\nabla \cdot \mathbf{B}) \mathbf{V}, \quad (19)$$

and

$$\begin{aligned} \frac{\partial \mathcal{E}}{\partial t} = & -\nabla \cdot \left[ \left( \mathcal{E} + P_g + \frac{B^2}{8\pi} \right) \mathbf{V} - \frac{1}{4\pi} \mathbf{B} (\mathbf{V} \cdot \mathbf{B}) \right] \\ & - \varrho \mathbf{V} \cdot \mathbf{g} - (\nabla \cdot \mathbf{B}) (\mathbf{V} \cdot \mathbf{B}). \end{aligned} \quad (20)$$

The variables  $\varrho$ ,  $\mathbf{V}$ ,  $\mathbf{B}$ ,  $P_g$ ,  $\mathcal{E}$ ,  $t$ ,  $\mathbf{g}$ , and  $\gamma$  are for the mass density, velocity of plasma flow, vector of the magnetic field, gas pressure, energy density ( $=\varrho V^2/2 + P_g/(\gamma - 1) + B^2/(8\pi)$ ), time, constant gravity of the Sun ( $= 274 \text{ m s}^{-2}$ ), and specific heat ratio, respectively. A colon between two vectors ( $\cdot : \cdot$ ) stands for the operation of the dyadic tensor product.

The terms with  $\nabla \cdot \mathbf{B}$  are added to the right-hand side except the continuity equation, in order to reduce the effects of the numerical nonzero divergence of the magnetic field (e.g., Brackbill & Barnes 1980; Powell 1994). The numerical divergence of the magnetic field is reduced with a partial divergence cleaner (see Hayashi 2005). The specific heat ratio  $\gamma$  is set constant and given as  $\gamma = 1 + \gamma_f$  with the fractional part  $\gamma_f$  set at  $1.0 \cdot 10^{-3}$  to mimic the near-isothermal circumstances in the solar corona. Under this near-isothermal assumption, the thermal energy density,  $P_g/(\gamma - 1) = P_g/\gamma_f$ , can be comparable to the magnetic energy density at strong magnetic field regions, which helps reduce the chance of computational failures due to the negative gas temperature. In the future, instead of the polytrope model, we would like to introduce physics-based descriptions of coronal heating and heat conduction (e.g., Usmanov et al. 2000, 2011; Mok et al. 2005; Bourdin et al. 2013), which are desirable and essential for realistic modeling.

The numerical schemes used here are mostly the same as those in our MHD code for the global solar corona and solar wind (Hayashi 2005; Hayashi et al. 2008), where several commonly used concepts and strategies, such as the Total Variation Diminishing (e.g., Harten 1983; Brio & Wu 1988), Monotonic Upstream Scheme for Conservation Laws (van Leer 1979), and Finite Volume Method (e.g., Tanaka 1995), are used. The Courant–Friedrichs–Levy number is set to 0.4, and computational parallelism is achieved by using MPI and OpenMP.

The Cartesian simulation region has six boundary surfaces, all of which are sub-Alfvénic. For the bottom-boundary surface on which the initial magnetic field and time-dependent electric field are specified, we assume that the plasma density and temperature are fixed and uniform all through the simulation. For further simplification, the plasma flow on the bottom boundary is set to be zero everywhere so that the sinusoidal condition (e.g., Yeh & Dyer 1985) can be always satisfied without any further treatments.

To drive the bottom-boundary magnetic field with the calculated electric field, the induction Equation (19) is replaced with

$$\frac{\partial \mathbf{B}}{\partial t} = -\nabla \times \mathbf{E}, \quad (21)$$

where the electric field at the right-hand side is the sum of all three parts,  $\mathbf{E} = \mathbf{E}^{(1)} + \mathbf{E}^{(2)} + \mathbf{E}^{(3)}$ . It must be mentioned that this replacement results in the violation of the conditions of an ideal frozen-in MHD system. It is desirable and important to include information on photospheric plasma motions to improve the estimate of the electric field as well as the

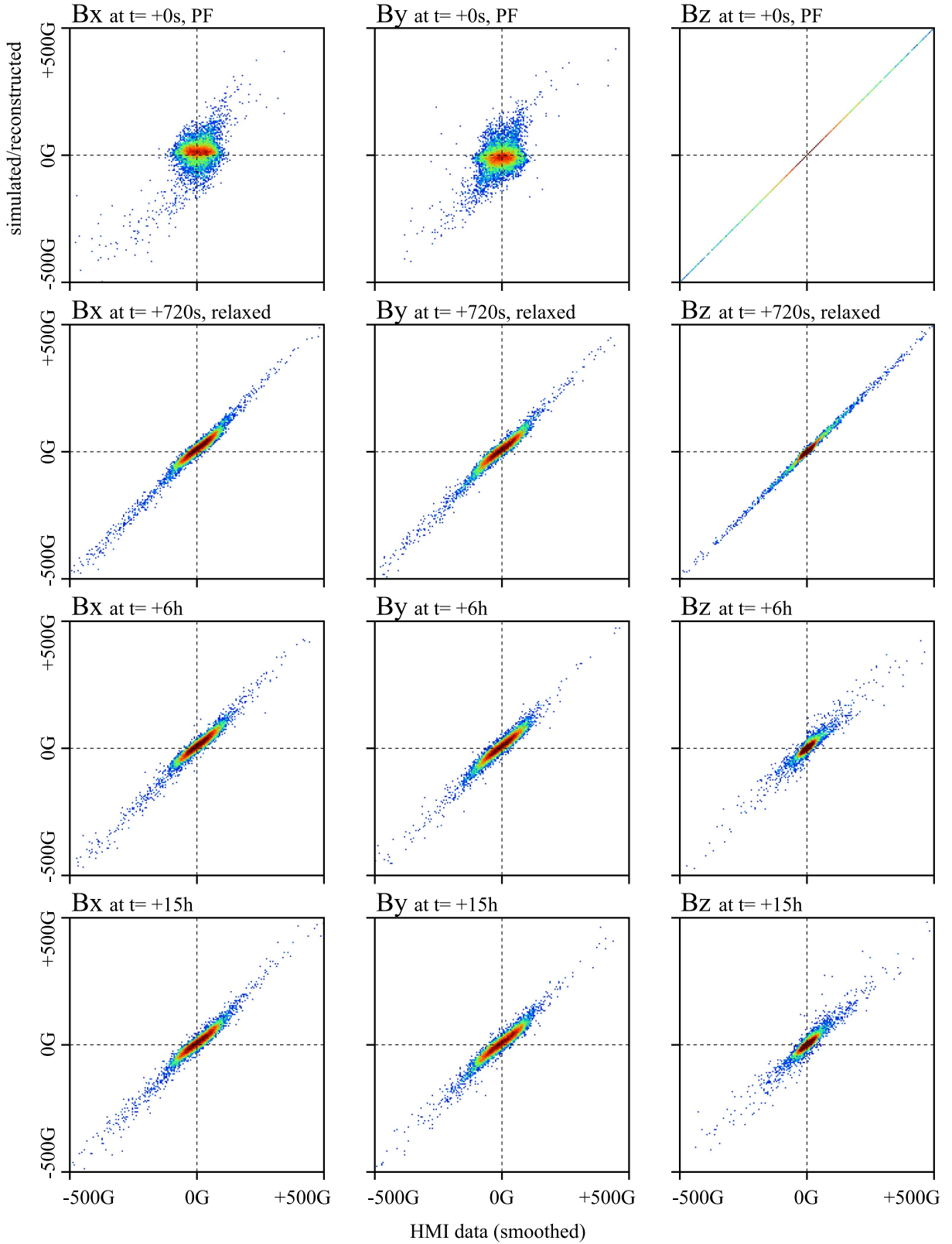


**Figure 4.** Scatter plots of the simulated and input magnetic field components ( $B_x$ ,  $B_y$ , and  $B_z$ ) on the bottom-boundary surface, within  $\pm 500$  G, at  $t = 0$ ,  $t = +720$  s,  $t = +6$  hr, and  $t = +15$  hr. The numbers of simulation grid points with values rounded to multiples of 5G are presented in logarithmic scale with colors, blue for  $10^0$ , green for  $10^1$ , and dark brown for  $10^2$ . In the E1 simulation step ( $0 \leq t \leq 720$  s), the horizontal components are altered from those of the potential field to the observation-based input values at  $t = +720$  s by the given electric field through the induction equation. The cumulative errors (scatters) at  $t = +6$  hr and  $t = +15$  hr are noticeable but reasonably small (the standard deviations of the differences are less than 10 G at  $t = +15$  hr).



Bz

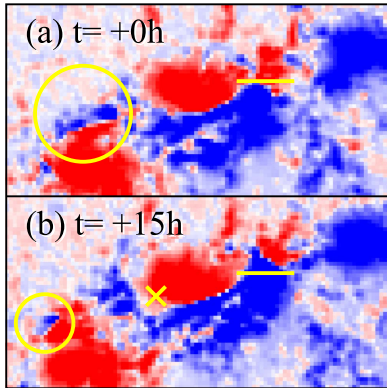


**Figure 5.** Enlarged maps of the vertical component of the simulated magnetic field ( $B_z$ ) near the central part of the AR at times  $t = 0$  and  $t = +15$  hr. A horizontal yellow line and a circle are placed, at the same positions in panels (a) and (b), to highlight the evolution. In panel (b), a yellow cross is placed at the position where the simulated data are sampled for Figure 13.

injection of kinetic energy, mass, and momentum into the transition region and corona (e.g., Fisher et al. 2012).

One would want to use a free boundary condition on the four side boundary surfaces rather than the periodic, mirror, or insulator boundary condition, because these non-free boundary conditions can distort the initial magnetic field configuration and hence substantially affect the simulation results. In our present model, we applied a modified version of the projected normal characteristic method (e.g., Nakagawa & Steinolfson 1976; Nakagawa et al. 1987; Wu & Wang 1987) to the rest of the five (side and top) boundary surfaces, in order to set up a proper sub-Alfvénic free boundary condition. The projected normal characteristic method is a physics-based boundary treatment used in various studies of solar ARs and the global corona (e.g., Wu et al. 1996, 2006, 2012; Feng et al. 2012; Yang et al. 2012). Without properly satisfying the characteristic equation system, unphysical quantities at the ghost cells (outside the simulation region) can enter the computation region and affect the simulated variables, and the physical and mathematical incompatibility (or inconsistencies) can subsequently lead to computational instabilities and unphysical vibrations with large amplitude.

The practical form of the free boundary treatment is given in Appendix B. In brief, in the projected normal characteristic method, the temporal variations derived with the ordinary difference method are decomposed into eight characteristic equations. Then, the characteristic equations for non-physical incoming waves are discarded (on the sub-Alfvénic surface, at least one wave mode is incoming), and the temporal variations on the boundary surface are reconstructed from only the outgoing wave modes. These mathematical operations use left and right eigenmatrices (or a set of left and right eigenvectors) of the hyperbolic MHD system, which are identical to the one commonly used in the Godunov-type linearized Riemann solver (e.g., Cargo & Gallice 1997).

To examine the capability of the free boundary treatment, we conduct a test simulation in which a plasma perturbation is given to the center of the simulation region with the initial value setting (described in the next section) to examine how well the induced pulse is treated. Figure 7 shows the vertical component of the plasma flow,  $V_z$ , in the  $z$ - $t$  diagram derived from this test simulation. No noticeable reflections can be seen

at the top boundary where the free boundary treatment is applied. The same non-reflective boundary condition is achieved on the four side boundary surfaces, too.

#### 4.2. Simulation Settings and Initial Values

In this paper, the temperature and hydrogen atom (proton) number density are set as  $T_0 = 2MK^\circ$  and  $N_0 = 10^{12} \text{ cc}^{-1}$ , respectively, on the bottom-boundary surface (at  $z = 0$  km). The simulated variables are normalized (nondimensionalized) with the factors  $V_0 (= \sqrt{2\gamma k_b T_0 / m_p} = 182.6 \text{ km})$  for velocity,  $t_0 (= Z_0 / V_0 = 490.7 \text{ s})$  for time, and  $B_0 (= \sqrt{8\pi\gamma N_0 k_b T_0} = 83.3 \text{ Gauss})$  for magnetic field, where  $k_b$  and  $m_p$  are the Boltzmann constant and mass of proton, respectively.

With the near-isothermal polytropic setting (with  $\gamma \sim 1$ ), the assumed temperature ( $2MK^\circ$ ) and substantially smoothed boundary magnetic field distributions, this present simulation study primarily simulates the lower corona above the solar transition region. This simulation setting allows us to avoid tentatively including computationally expensive components, such as physics processes with very short timescales (e.g., heat conduction, radiation, ionization and opacity, and Alfvén wave decays) and very steep vertical gradients of plasma quantities. The solar transition region is of great importance for estimating thermal and kinetic fluxes, and for better, more realistic simulations, we would try to include it in the future.

In many simulation models of the global solar corona, the plasma number density is typically set to be  $10^8 \text{ counts cc}^{-1}$ . However, with the number density of  $10^8 \text{ counts cc}^{-1}$ , the Alfvén speed at a typical 1000 G magnetic field is about 0.3 of the speed of light, and unfortunately, our time-dependent MHD simulation model cannot handle such high Alfvén speed and low beta regime. After several provisional tests, we chose a much larger number,  $10^{12} \text{ counts cc}^{-1}$ , as a compromise for mitigating computational difficulties. With this value of the number density, a typical smallest value of the  $\beta$  ratio is about  $1/400$  at a 1700 G field (99th percentile  $|B|$  over all resized data maps used), and the Alfvén speed at 1000 G field (96th percentile strength) is reduced to the order of  $10^3 \text{ km s}^{-1}$ .

The grid sizes in the vertical direction  $\Delta z$  is set equal to that in the horizontal direction ( $\Delta x = \Delta y = 1400 \text{ km}$ , i.e., four times as large as the original HMI SHARP data grid size). The number of simulation grid cells in the  $x$ ,  $y$ , and  $z$  directions is  $186 + 30 \times 2$ ,  $64 + 30 \times 2$ , and 64, respectively, with a 30 grid width horizontal buffer where we place zero values of the magnetic field and electric field on the bottom-boundary surface. This buffer is set to avoid complex treatments at the edges and corners of the bottom-boundary surface. The sizes of the simulation region in the  $x$ ,  $y$ , and  $z$  directions are, hence, 354,240 km ( $X_0 = 246\Delta x$ ), 178,560 km ( $Y_0 = 124\Delta y$ ), and 89,600 km ( $Z_0 = 64\Delta z$ ), respectively.

The initial plasma is at hydrostatic equilibrium under constant solar gravity. The initial magnetic field is the PF that is calculated through an iterative, three-dimensional Laplace solver,

$$\frac{\partial \Phi}{\partial \tau} = \nabla \cdot \nabla \Phi, \quad (22)$$

with the boundary conditions  $\partial_z \Phi = -B_z$  on the bottom-boundary surfaces (at  $z = 0$ ) and  $\partial_{x_i}^2 \Phi = 0$  ( $x_i = \{x, y, z\}$ ) on the other side and top boundary surfaces. The values of the



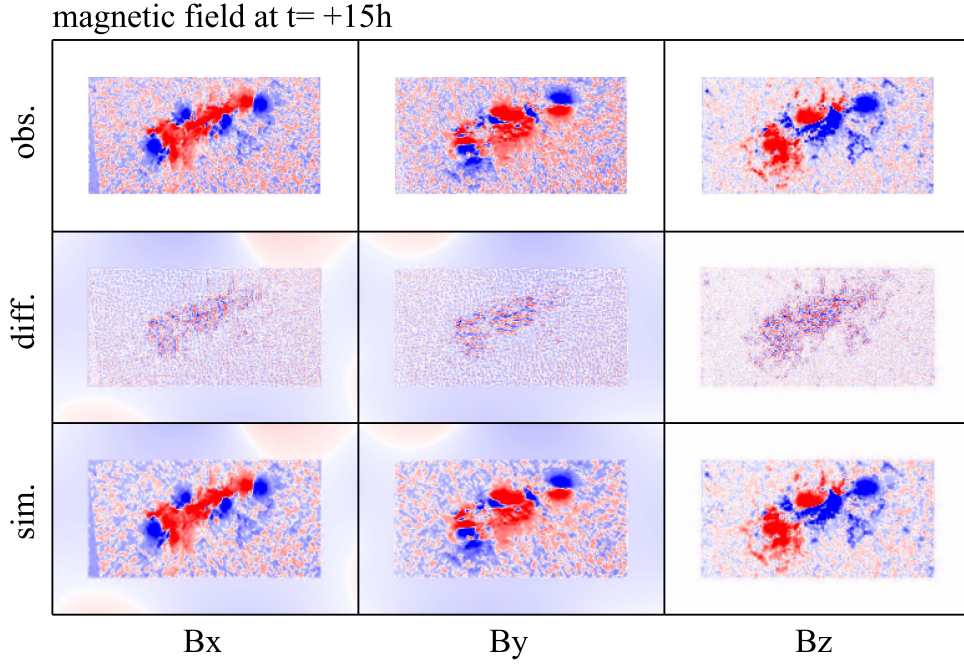


**Figure 6.** Maps of the three components of the magnetic field at  $t = +15\text{ hr}$ . The smoothed observation data are shown in the top row, and the simulated magnetic field is shown in the bottom row. In the middle, the differences between the two are shown. The colors (blue for positive polarity, and red for negative polarity) are proportional to the square root of the absolute values and truncated at 500 G. Small nonzero values of the simulated  $B_x$  and  $B_y$  at the buffer regions are due to the nonzero initial values of the PF.

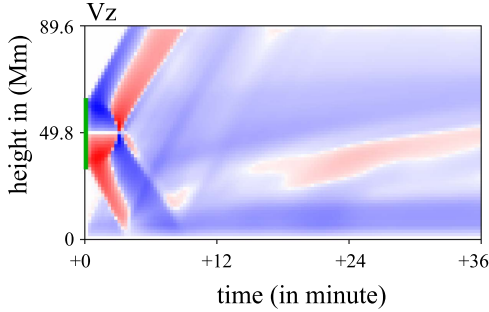


**Figure 7.** Time–height ( $t$ – $z$ ) diagram of  $V_z$  derived from the simulation for testing the ability of the projected normal characteristic method applied to the top sub-Alfvénic boundary surface. The blue (red) color stands for upward (downward)  $V_z$ . A spherical perturbation (five-times enhancement of the plasma pressure or temperature) is given at the center of the simulation box. The size and height of the perturbation are denoted with a thick green line at the leftmost part of the plot. The explosion and implosion flows generated by the perturbation pass through the sub-Alfvénic top boundary without any noticeable reflections.

potential scalar  $\Phi$  are placed at the centers of the cell face in the vertical direction,  $(i\Delta x, j\Delta y, (k + 1/2)\Delta z)$ , so that the observation-based boundary  $B_z$  can be straightforwardly introduced as the boundary condition on the bottom boundary. The PF vector is calculated as the gradient of the scalar potential,  $\mathbf{B} = -\nabla\Phi$ .

#### 4.3. Simulation Steps

The horizontal components of the initial PF configuration on the bottom boundary do not match the observation data. Hence, in order to simulate the AR system as realistically as possible, we introduced the three steps of the simulation as follows. In the first step (hereafter labeled as the E1 step), starting with the PF, we simulate the MHD variables with the  $\mathbf{E}$ -driven

simulation for 720 s, using the electric field vector maps derived from the difference between the PF vector (whose  $B_z$  are identical to the observation) at  $t = +0\text{ s}$  and three components of the magnetic field data map at  $t = +720\text{ s}$ . At  $t = +720\text{ s}$ , all three components of the magnetic field on the bottom boundary become almost the same as those of the observed data map at  $t = +720\text{ s}$ , as seen in plots in Figure 4. In the second step (hereafter labeled the E0 step), the  $\mathbf{E}$ -driven simulation is continued but with zero electric field,  $\mathbf{E} = 0$ , until the simulated system reaches a well-relaxed state (with the largest residual plasma motion of 0.01 Alfvén speed). Because the bottom-boundary magnetic field is fully controlled by the given  $\mathbf{E}$ , all three components of the boundary  $\mathbf{B}$  are fixed throughout this step. In the third step (hereafter labeled the E2-step), the  $\mathbf{E}$ -driven simulation (identical to the E1 step, except for values of the boundary  $\mathbf{E}$ ) restarts from the relaxed state with the observation-based (nonzero) electric field to simulate the AR system responding to the variation of the observed solar photospheric magnetic field at  $t > +720\text{ s}$ . Within each 720 s interval over the 16 hr period, the given electric field is fixed. When the simulated time  $t$  reaches the end of each interval, the time step is adjusted so that the total time will be exactly a multiple of the HMI data interval.

To speed up the simulations, we increase the magnitude of the boundary electric field by a factor of five, and instead shorten the simulation interval from 720 to 144 s. This shortened interval is shorter than the normalization factor of time,  $t_0 = 490.7\text{ s}$ , which is equal to the Alfvén speed for a typical magnetic field strength ( $B_0$ ) and density ( $N_0$ ). Because the magnetic field at the central part of the sunspot region is stronger than  $B_0$ , the travel time of Alfvén waves across the simulation box is comparable to or shorter than 144 s. Furthermore, the characteristic-based boundary treatments have significantly reduced wave reflections at the sub-Alfvénic boundary surfaces, and hence the influence of this speed-up

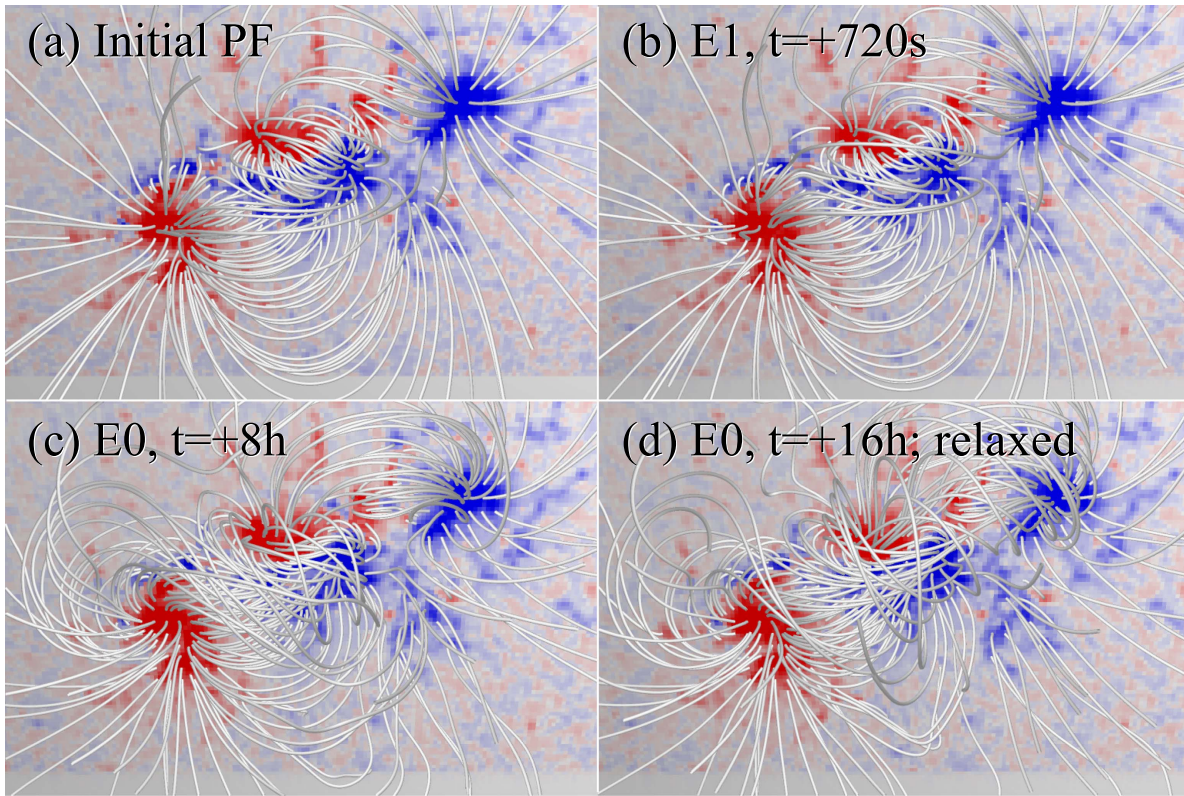


**Figure 8.** Magnetic field lines at (a) the initial state (PF configuration), (b) the end of the E1 step, (c) the middle of the E0 step, and (d) the end of the E0 step. Through step E1, the initial PF magnetic field structure is altered due to the electric field. The related state in panel (d) displays many noticeable features, such as twisted field lines near the main PIL and expanded overlying field lines in the surrounding regions, generated through the E0 step. The viewpoint is set  $15^\circ$  northward off from the top direction, in order to mimic the view of the AR in the solar southern hemisphere seen from the Earth.

trick is minimized. Therefore, the generality of the magnetic field and plasma quantities will be well preserved.

### 5. Simulation Results

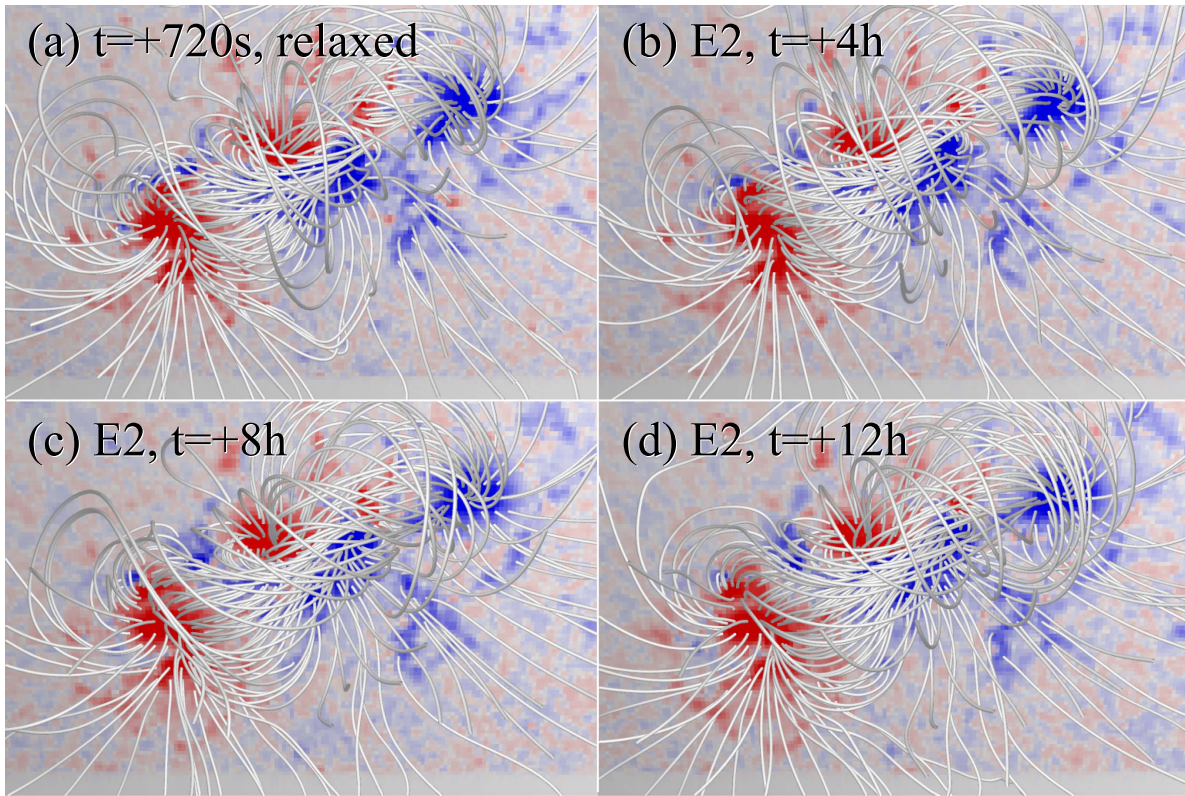
In this section, a few features noticeable in the simulation result data derived through steps E0, E1, and E2, are demonstrated.

Figure 8 shows the simulated magnetic field lines in the course of the E1 and E0 steps. Starting with the PF configuration, the simulated magnetic field gradually gains non-potential features, such as twists, particularly around the primary polarity inversion line (PIL; near the center of the boundary data maps). The magnetic field in the surrounding regions also displays the changes in connectivity region to a large scale; some field lines starting from a large spot region to the side boundary surfaces in the PF solution reach the region of the other polarity on the bottom-boundary surface, for example. Overall, the amount of magnetic flux closed within the simulation region increases in comparison with the PF, minimum-energy state. It is probable that the magnetic field structures of the relaxed state (plot (d)) are substantially different from the NFLLL or other force-free solutions; the time-dependent MHD model, in an ideal case, retains the connectivity in the course of the simulation run (except for the changes caused by the numerical viscosity). Hence, our setting (of the initial PF configuration) actually defines in advance many aspects of the resultant relaxed state. Nonetheless, the relaxed state (with residual plasma motion of about  $3 \text{ km s}^{-1}$  near the main PIL) is a suitable MHD state as a starting point of the E2  $E$ -driven steps for  $t > 720 \text{ s}$ .

The temporal evolution of magnetic field lines at  $t \geq 720 \text{ s}$  (in the simulation step E2) is shown in Figure 9, in the same format as in Figure 8. As shown in Figure 5, the variations of the solar-surface magnetic field over the 16 hr period are not substantially large on a global scale, and hence the overall evolution of the magnetic field lines is not noticeably large. Still, as shown in Figure 10, the magnetic field near the primary PIL changes substantially: weakly twisted features of relatively short field lines at  $t = +720 \text{ s}$  are gradually stretched along the PIL, and horizontal field lines already elongated at  $t = +720 \text{ s}$  are kept aligned along the PIL.

The plasma flow velocity ( $\mathbf{V}$ ) and current density ( $\mathbf{J} = \nabla \times \mathbf{B}$ ) are important in the dynamics of the AR system. Figure 11 shows the simulated plasma velocity ( $\mathbf{V}$ ), magnetic field ( $\mathbf{B}$ ), and the current density ( $\mathbf{J} = \nabla \times \mathbf{B}$ ) at  $z = 7000 \text{ km}$  (fifth from the bottom-boundary surface) and  $t = +4 \text{ hr}$ . In plots (a) and (b), the horizontal components of the plasma flow exhibit somewhat complicated distributions near the center. On the other hand, the vertical component is rather organized: in plot (c), plasma motions that are upward (positive  $V_z$ , blue-colored in plot) in the northern (upper) half and downward (red-colored) in the southern part are noticeable. This tendency is more clearly seen near the center, where the upward motions in the region of negative  $B_z$  and downward motions in positive  $B_z$  are seen. This is because the magnetic field evolution is not even over the main PIL at earlier times. The magnetic field components become rather smoothed in comparison with the bottom-boundary distributions; however, some faint spiral lanes of a stronger field emanating from large strong-field regions are noticeable. Such small-scale magnetic





**Figure 9.** Same as in Figure 8, except for the simulation data at (a)  $t = +720$  s, (b)  $t = +4$  hr, (c)  $t = 8$  hr, and (d)  $t = +12$  hr, over the course of the E2 simulation step. Panel (a) is identical to panel (d) in Figure 8.

field structures are responsible for the current distributions in plots (g)–(i), where the current distributions are roughly aligned along the magnetic field distributions. These features derived with a time-dependent three-dimensional full MHD model will help enhance our understanding of the dynamics of the AR system.

Figure 12 shows the temporal evolution of the magnetic energy integrated over a one-eighth volume of the simulation region,  $\{(1/4)X_0 \leq x \leq (3/4)X_0, (1/4)Y_0 \leq y \leq (3/4)Y_0, 0 \leq z \leq (1/2)Z_0\}$ . As references, the quantities of the PF ( $B_p$ ) with identical bottom-boundary  $B_z$  maps are calculated for each instant. The difference between the total and potential energy,  $\int (B^2 - B_p^2) dV / 8\pi$ , or free magnetic energy, around the central part of the AR system is about  $2 \cdot 10^{32}$  erg, which is comparable to  $2.0\text{--}2.8 \cdot 10^{32}$  erg as estimated by Kazachenko et al. (2015) and Sun et al. (2012). The simulation results did not show noticeable sudden decreases in the total or free magnetic energy at the time of the X-class flare event. The reference PF energy did not show substantial temporal variations over the simulated period, and only a small dip in the PF total energy is noticeable at the time of the X-class flare.

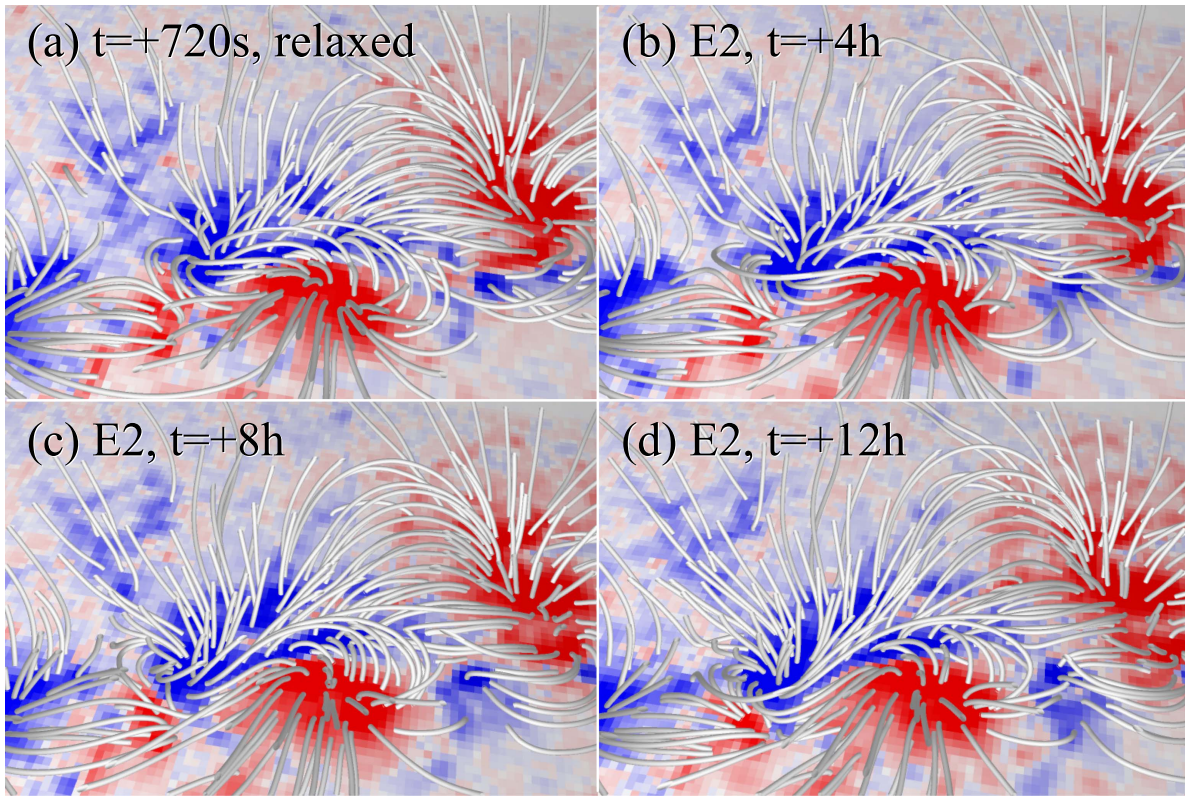
The photospheric magnetic field was substantially altered by the X-class flare event (e.g., Sun et al. 2017), and the first noticeable change in the 12 minute cadence HMI data is found on 2011 February 15 02:00 UT. A data-driven model like the present MHD model simulates the responses of the solar corona to sudden variations in the boundary data, which are consequences perhaps of the flare (or other impulsive) event above the photosphere in the actual Sun. In this cause and consequence framework, in principle, the data-driven model cannot reproduce the flare event and its photospheric consequences.

Figure 13 shows the time–height ( $t$ – $z$ ) diagram of the simulated plasma density and a horizontal component of the magnetic field, sampled at the position marked with the yellow cross in Figure 5. The selected data sample position is the approximate center of the region where the horizontal components of the HMI vector magnetic field exhibits a sudden and irreversible enhancement immediately after the X-class flare event. In this  $z$ – $t$  plot, a surge of lower density and positive  $B_y$  emerges out of the lowermost part of the simulation region and moves up to the middle height of the simulation box. Because the speed of the surge is estimated to be about  $2.5 \text{ km s}^{-1}$  (or  $5 \text{ Mm/6 hr}$ ; about 1% of the local sound speed), the surge represents the reconfiguration of the global magnetic field, rather than some sort of shock wave from the flare site or the impacted solar surface.

## 6. Summaries and Discussions

In this paper, we describe our time-dependent three-dimensional MHD model for the data-driven simulation of a sub-Alfvénic solar AR. As a test, we carried out the simulation of a solar AR, NOAA 11158. Using HMI vector magnetic field observation data, we calculate the boundary driving  $\mathbf{E}$  for this region by means of a simple and practical algorithm that only uses a two-dimensional Poisson solver. The calculated (inversed) boundary  $\mathbf{E}$  can successfully reproduce the observed temporal evolution of the (smoothed) solar photospheric magnetic field. The results of the three-dimensional time-dependent MHD simulation exhibit reasonable behaviors of the magnetic field and plasma. The evolution of the simulated magnetic field energy agrees reasonably well with other independent analyses of the observation data. These suggest





**Figure 10.** Magnetic field lines near the main PIL, at (a)  $t = +720$  s, (b)  $t = +4$  hr, (c)  $t = +8$  hr, and (d)  $t = +12$  hr. For visibility, the viewpoint is set  $10^\circ$  off from the solar north direction (the y-axis direction of the simulation system) and  $45^\circ$  off from the top (z-direction), and only the field line segments in the lowermost part ( $z \leq 7000$  km) are drawn.

that the simulation framework employed in this study is reasonably organized and can be a foundation and a basic step toward more realistic modeling of solar ARs to help enhance our understanding of the dynamics of AR system, in particular magnetic energy build-up processes and the sudden release of magnetic energy (i.e., flares).

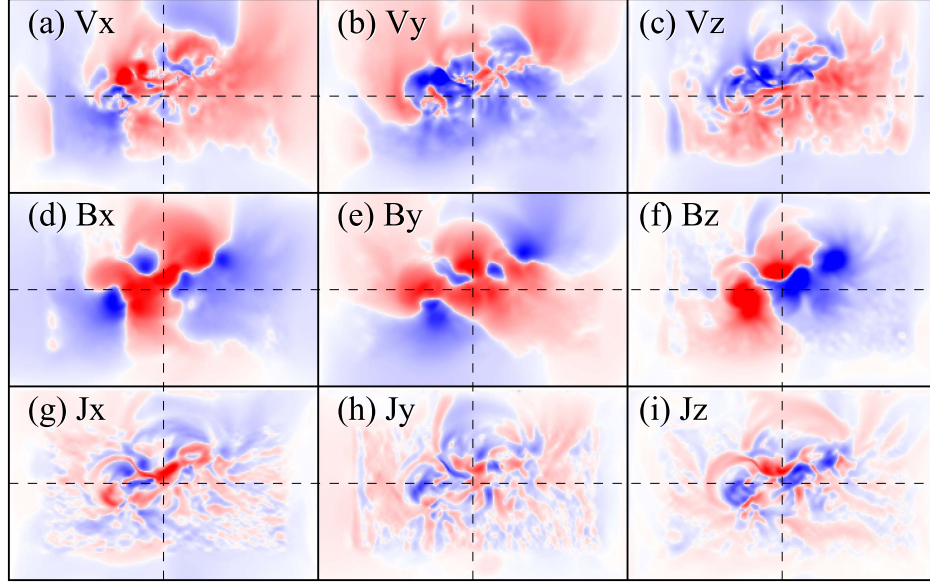
In the following, we address the issues and desired functionalities for future improvements.

With the current settings, the sudden magnetic energy release was not reproduced, in part because the basic equations do not include the magnetic resistivity, but mainly because the time-dependent boundary data do not have any information about when and where such events happened. In data-driven simulation models for ARs, we often assume that the solar-surface magnetic field is the cause of coronal phenomena. In fact, however, the input data for the bottom sub-Alfvénic boundary surface contain information on both causes of and influences from coronal events above the photosphere, and we do not have any immediate procedures to distinguish the two. The characteristic-based approach we used for treating the sub-Alfvénic surfaces can distinguish between the incoming and outgoing MHD waves passing through a surface, but this capability is generally limited to the simulated variables and cannot work for the given observation-based boundary values. It is desirable to have a method, based on the concept of characteristics, or is physics or mathematics based, capable of filtering the photospheric causes (incoming information toward the corona) and influences (outgoing information from the corona above) in the observation data of the photosphere.

In principle, the simulated sub-Alfvénic system can retain memory, at least partially, of the initial value setting that often

contains many assumptions. For example, in the present simulation study, the connectivity of the magnetic field lines (e.g., whether two points on the photosphere were magnetically connected or one end of the field line reaches the side or top boundary surface) in the initial PF configuration is, at least partially, kept over the 16 hr simulated period. One reasonable approach to minimize the influence of this memory effect is to start the simulation from a much earlier time, as in the work of Jiang et al. (2016) where the simulation starts before the emergence of AR sunspots. The use of sophisticated three-dimensional AR magnetic field modeling, such as NLFFF or NFFF, as the initial value will be beneficial, too.

The bottom-boundary electric field calculated with our practical approach can reproduce the temporal evolution of the observed vector magnetic field. However, we need to be careful about a few points when using the method for purposes other than data-driven simulation. The calculated  $\mathbf{E}$  is not guaranteed to be always perpendicular to  $\mathbf{B}$ , and no specific attention or aids were placed on the gauge uncertainty. In addition, the method is designed to yield the  $\mathbf{E}$  assigned at different positions. This is a convenient and suitable choice for the differencing methods; however, it is perhaps not suitable for analyzing and diagnosing the physics conditions on a particular layer. For example, for the second part ( $\mathbf{E}^{(2)} = \hat{\mathbf{z}}\Psi^{(2)}$ ), the scalar potential  $\Psi^{(2)}$  can be added to any arbitrary integration constant. In addition, the third part ( $\mathbf{E}^{(3)}$ ) is set zero at height  $z = 0$ ; hence, the surface electric field vectors are not adequate for estimating the Poynting flux (when expressed as  $\mathbf{E} \times \mathbf{B}$ ) on the bottom boundary. The determined electric field vectors would be, nonetheless, useful for determining the (temporal evolution of) vector potential, as

vector quantities at  $z=7000$  km,  $t=+4$ h

**Figure 11.** Distribution of the three components of (a)–(c) the plasma flow velocity  $\mathbf{V}$ , (d)–(f) magnetic field  $\mathbf{B}$ , and (g)–(i) current density  $\mathbf{J}(=\nabla \times \mathbf{B})$  on the  $x$ – $y$  plane at a height  $z = 7000$  km ( $= 5 \cdot \Delta z$ ). Dashed lines are placed to assist in comparisons. Blue and red colors represent positive and negative values, respectively, and the colors are truncated at  $\pm 5$  km s $^{-1}$  for the velocity,  $\pm 300$  G for the magnetic field, and  $\pm 0.15$  G km $^{-1}$  for the current density.

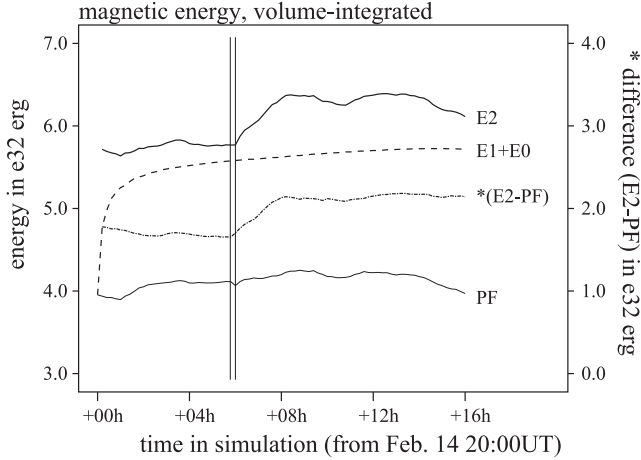


**Figure 12.** Temporal evolution of the magnetic energy integrated over the selected part of the simulation region,  $\{x, y, z | (1/4)X \leq x \leq (3/4)X, (1/4)Y \leq y \leq (3/4)Y, 0 \leq z \leq (1/2)Z\}$ . The dashed curve (labeled E1+E0) is for the total energy over the course of the first two simulation steps, and the thick solid line (labeled E2) is for the evolution obtained in step E2. The energy of the potential field (PF) with bottom-boundary maps identical to those in the E2 simulation step is shown with a thin solid line. The dashed–dotted curve is for the difference between the energy of the E2 simulation step and that of the reference potential field. The two vertical lines are placed at the approximate time of the X-class flare event (left) and at the time 02:00 UT (right).

$\partial_t \mathbf{A} = -\mathbf{E}$ , and estimating, with caution, the magnetic helicity ( $\mathbf{A} \cdot \mathbf{B}$ ).

In determining the third part of the electric field (Equations (12) and (14)), we assumed that the surplus (convergence) of horizontal components of the magnetic field ( $\nabla_h \cdot \mathbf{B}_h$ ) is evenly redistributed to the upward  $B_z$  on the upper cell face and to the downward  $B_z$  on the lower face. This assumption is equivalent to explicitly giving the vertical gradient of the magnetic field and hence its temporal variation. In the MHD system and the actual corona, the vertical gradient

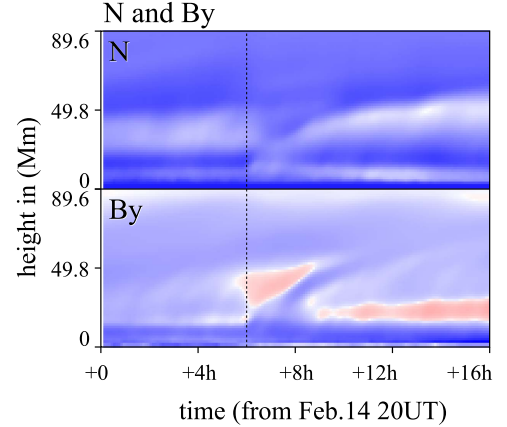


**Figure 13.** Time–height ( $t$ – $z$ ) diagram of the plasma density (top) and  $B_y$  (bottom), sampled at the selected position where substantial changes of the magnetic field values had been observed immediately after the X-class flare event. The sampling position is shown with a cross in Figure 5.

and, in particular, the advection term (with respect to the vertical direction,  $-V_z \partial_z \mathbf{B}$ ), are critically important in estimating the magnetic flux and energy flux supplied through the photosphere into the solar corona (e.g., Leka et al. 1996; Fisher et al. 2012); hence, determining the gradient properties in an observation-based manner is desired. Several analysis methods mentioned in Section 1 as well as the Doppler velocity observation can help determine the values of  $V_z$ , although we need extra effort to determine the vertical gradients. For example, advanced analysis methods (e.g., Frutiger et al. 2000) can infer the vertical gradients from spectroscopic measurements through the Stokes inversion. Even from the HMI filtergram measurement, the line-of-sight components of the magnetic field and Doppler velocity at three different heights can be retrieved (e.g., Nagashima et al. 2014). Perhaps simultaneous multi-line observations of the solar surface will



offer direct descriptions of photospheric vertical gradients. One of our plans is to coordinate with these observations and analysis methods in order to introduce new observation-based constraints to the algorithms and improve the entirety of simulation model. For example, we can evaluate and judge whether Equation (10) is adequate and learn how to select the optimal size of the grid cell in the vertical direction ( $\Delta z$  is the only arbitrary parameter in determining the electric field) such that we can minimize the discrepancy in Equation (10). We hope to develop a new boundary model capable of introducing straightforwardly such observation-based information as constraints on the time-dependent boundary values in the future.

We thank the anonymous referee for helpful comments and suggestions. We use the vector magnetic field data taken by the HMI and the coronal plasma image data by the AIA on board the *SDO* that are publicly available through <http://jsoc.stanford.edu/ajax/lookdata.html>. The *SDO* data are courtesy of NASA and the *SDO* science team. This work is partially supported by the computational joint research program of the Institute for Space-Earth Environment Research, Nagoya University, Japan, and some computations for this study were conducted on the CX400 and FX100 supercomputer systems at the Information Technology Center, Nagoya University. The authors are jointly supported by the National Natural Science Foundation of China (grant Nos. 41374175, 41531073, 41574171, and 41731067) and the Specialized Research Fund for State Key Laboratories.

Facility: *SDO* (HMI, AIA).

### Appendix A Calculations of the Temporal Derivatives of the Magnetic Field on the Bottom Boundary

The temporal variation of the vertical component of the magnetic field,  $\partial_t B_z$ , is determined as the minus curl of the first electric field,  $\mathbf{E}^{(1)}$ ,

$$\begin{aligned} \frac{\partial B_z}{\partial t} &= -\hat{\mathbf{z}} \cdot (\nabla \times \mathbf{E}^{(1)}) = -\hat{\mathbf{z}} \cdot [\nabla \times (\hat{\mathbf{z}} \times \nabla_h \Psi^{(1)})] \\ &= -\hat{\mathbf{z}} (\nabla_h \cdot \nabla_h \Psi^{(1)}) = B_z'. \end{aligned} \quad (23)$$

The temporal derivatives of the divergence-free part of the horizontal components of the boundary magnetic field are calculated as

$$\begin{aligned} \frac{\partial \mathbf{B}_{h,df}}{\partial t} &= -\nabla \times \mathbf{E}^{(2)} = -\nabla \times (\hat{\mathbf{z}} \Psi^{(2)}) = -\hat{\mathbf{z}} \times \nabla_h \Psi^{(2)} \\ &= \left( \frac{\partial \Psi^{(2)}}{\partial y}, -\frac{\partial \Psi^{(2)}}{\partial x}, 0 \right). \end{aligned} \quad (24)$$

The agreements between the divergence-free horizontal vectors are confirmed by comparing an identity form,

$$\nabla_h^2 \Psi^{(2)} + \frac{\partial}{\partial x} \left( -\frac{\partial \Psi^{(2)}}{\partial x} \right) - \frac{\partial}{\partial y} \left( \frac{\partial \Psi^{(2)}}{\partial y} \right) = 0, \quad (25)$$

with the Poisson Equation (9),

$$\nabla_h^2 \Psi^{(2)} + \hat{\mathbf{z}} \cdot (\nabla_h \times \mathbf{B}_{h,df}') = \nabla_h^2 \Psi^{(2)} + \frac{\partial B_y'}{\partial x} - \frac{\partial B_x'}{\partial y} = 0. \quad (26)$$

The Maxwell equation for the curl-free part of the horizontal magnetic field components,

$$\begin{aligned} \partial_t \mathbf{B}_{h,cf} &= -\nabla \times \mathbf{E}^{(3)} = \nabla \times (\hat{\mathbf{z}} \times (\nabla_h \Psi^{(3)})) \\ &= \nabla \times \left( \frac{\partial \Psi^{(3)}}{\partial y}, -\frac{\partial \Psi^{(3)}}{\partial x}, 0 \right), \end{aligned} \quad (27)$$

can be rewritten as

$$\partial_t \mathbf{B}_{h,cf} = -\frac{2}{\Delta z} \nabla_h \Psi^{(3)} \quad (28)$$

through differencing form presentations,

$$\begin{aligned} \frac{\partial B_x^{(3)}}{\partial t} \bigg|_{z=0} &= +\frac{\partial E_y}{\partial z} = \frac{E_y^{(3)}|_{z=+\Delta z/2} - E_y^{(3)}|_{z=-\Delta z/2}}{\Delta z} \\ &= \frac{2}{\Delta z} E_y^{(3)} = -\frac{2}{\Delta z} \frac{\partial \Psi^{(3)}}{\partial x}, \end{aligned} \quad (29)$$

and

$$\begin{aligned} \frac{\partial B_y^{(3)}}{\partial t} \bigg|_{z=0} &= -\frac{\partial E_x}{\partial z} = -\frac{E_x^{(3)}|_{z=+\Delta z/2} - E_x^{(3)}|_{z=-\Delta z/2}}{\Delta z} \\ &= -\frac{2}{\Delta z} E_x^{(3)} = \frac{2}{\Delta z} \frac{\partial \Psi^{(3)}}{\partial y}. \end{aligned} \quad (30)$$

From Equation (13), we obtain

$$\frac{\partial \mathbf{B}_h^{(3)}}{\partial t} \bigg|_{z=0} = \mathbf{B}_{h,cf}' + \mathbf{C}, \quad (31)$$

where  $\mathbf{C}$  is an arbitrary divergence-free horizontal vector. Performing a horizontal curl operation on both sides of Equation (31) yields  $\nabla_h \times \mathbf{C} = 0$ ; hence,  $\mathbf{C}$  is indeed a (unique) horizontal two-dimensional PF vector within a bounded area (data map). A tactic to minimize the magnitude of disagreement  $\mathbf{C}$  is to adjust the values of  $\mathbf{B}_h'$  on the outermost data points of the input photospheric magnetic field map in such a way that the total  $|\mathbf{C}|$  will be zero or greatly reduced. However, such an adjustment is usually very complicated, and may often alter the input data map substantially. In the present study, we do not include any aids to cancel or reduce this error, because the magnitudes of  $\mathbf{C}$  are order of 10 G per 12 minutes, much smaller than those at the center of the AR system. The HMI HAPR and SHARP modules choose bounding box sizes such that the horizontal components of the magnetic field at the outermost part of the clipped data map are very weak, mostly at the observation noise level. In addition, the magnitude of the error vector  $\mathbf{C}$  might be very small near the center of the bounded box (data map), because the contribution from data boundary pixels cancel out.



## Appendix B

### Characteristic-based Treatments for the Free Boundary Surface

Let us write the governing MHD equations in vector-matrix form,

$$\frac{\partial \mathbf{U}}{\partial t} = -\frac{\partial \mathbf{F}_i}{\partial x_i} + \mathbf{S}_i = -\frac{\partial \mathbf{F}_i}{\partial \mathbf{U}} \frac{\partial \mathbf{U}}{\partial x_i} + \mathbf{S}_i = -\mathbf{J} \frac{\partial \mathbf{U}}{\partial x_i} + \mathbf{S}_i, \quad (32)$$

where  $x_i$  is the direction normal to the boundary surface under consideration, and the vector  $\mathbf{F}_i$  is the flux vector in the  $x_i$  direction. The vector  $\mathbf{S}_i$  in the right-hand side contains all of the other terms, such as the flux gradients in the other directions and source terms. The Jacobian matrix  $\mathbf{J}$  of a hyperbolic MHD system can be rewritten as

$$\mathbf{J} = \mathbf{R}\mathbf{A}\mathbf{L}, \quad (33)$$

where  $\mathbf{R}$  and  $\mathbf{L}$  are the matrix form of the normalized right and left eigenvectors of the Jacobian  $\mathbf{J}$ , respectively. The matrix  $\mathbf{A}$  is a diagonal matrix of eigenvalues,  $\mathbf{A} = \text{diag}(\lambda_1, \lambda_2, \dots, \lambda_7)$ . The eigenvalues of the Jacobian  $\mathbf{J}$  of the MHD equation system are all real and equal to, in non-decreasing order,  $\lambda_1 = V_i - V_{F,i}$ ,  $\lambda_2 = V_i - V_{A,i}$ ,  $\lambda_3 = V_i - V_{S,i}$ ,  $\lambda_4 = V_i$ ,  $\lambda_5 = V_i + V_{S,i}$ ,  $\lambda_6 = V_i + V_{A,i}$ , and  $\lambda_7 = V_i + V_{F,i}$ , where the speed of the fast, Alfvén, and slow modes are given as  $V_{F,i} = \sqrt{(a^2 + b^2 + \sqrt{(a^2 + b^2)^2 - 4a^2b_i^2})/2}$ ,  $V_{A,i} = |b_i|$ , and  $V_{S,i} = \sqrt{(a^2 + b^2 - \sqrt{(a^2 + b^2)^2 - 4a^2b_i^2})/2}$ , with auxiliary variables  $a = \sqrt{P_g/\rho}$ ,  $b_i = B_i/\sqrt{4\pi\rho}$ , and  $b^2 = (B_i^2 + B_j^2 + B_k^2)/(4\pi\rho)$ . The three subscripts  $i$ ,  $j$ , and  $k$  recursively represent the directions in the Cartesian system,  $x$ ,  $y$ , and  $z$ . The eigenmatrices are normalized satisfying the normalization relationship,  $\mathbf{R}\mathbf{L} = \mathbf{L}\mathbf{R} = \mathbf{I}$  (Roe & Balsara 1996; Cargo & Gallice 1997; and also given in Hayashi 2005).

By operating on the left eigenmatrix  $\mathbf{L}$  from the left, Equation (32) becomes

$$\mathbf{L} \frac{\partial \mathbf{U}}{\partial t} = \mathbf{L} \left( -\mathbf{R}\mathbf{A}\mathbf{L} \frac{\partial \mathbf{U}}{\partial x_i} + \mathbf{S}_{x_i} \right) = -\mathbf{A}\mathbf{L} \frac{\partial \mathbf{U}}{\partial x_i} + \mathbf{L}\mathbf{S}_{x_i}, \quad (34)$$

The  $l$ th row,

$$L_{l1} \left( \frac{\partial}{\partial t} + \lambda_{l,i} \frac{\partial}{\partial x_i} \right) \varrho + L_{l2} \left( \frac{\partial}{\partial t} + \lambda_{l,i} \frac{\partial}{\partial x_i} \right) (\varrho V_i) + \dots + L_{l7} \left( \frac{\partial}{\partial t} + \lambda_{l,i} \frac{\partial}{\partial x_i} \right) \mathcal{E} = \sum_{m=1}^7 L_{lm} S_{r,m}, \quad (35)$$

or a reorganized form,

$$L_{l1} \frac{\partial \varrho}{\partial t} + L_{l2} \frac{\partial (\varrho V_i)}{\partial t} + L_{l3} \frac{\partial (\varrho V_j)}{\partial t} + L_{l4} \frac{\partial (\varrho V_k)}{\partial t} + L_{l5} \frac{\partial B_j}{\partial t} + L_{l6} \frac{\partial B_k}{\partial t} + L_{l7} \frac{\partial \mathcal{E}}{\partial t} = \text{RHS}_l, \quad (36)$$

represents the wave (or propagation of information) with speed  $\lambda_l$ .

On the sub-Alfvénic boundary surfaces, the temporal evolution of physics quantities must be determined only with the spatial gradients associated with the outgoing waves. Hence, for the free boundary surfaces, we have to use

information carried by the outgoing wave modes and exclude information carried by the incoming wave modes.


Here, we organize the free boundary treatment at the surface  $x_i = 0$  such that consistency is achieved by discarding the incoming unphysical eigenwave modes (with positive eigenvalues). Among some possible choices allowed in the concept of the projected normal characteristics approach, one can discard the unphysical incoming waves by simply resetting the right-hand side of Equation (36) with a positive eigenvalue  $\lambda_l$  to zero:

$$\text{RHS}_l^* = \begin{cases} 0 & \text{if } \lambda_l > 0 \\ \text{RHS}_l & \text{otherwise} \end{cases}. \quad (37)$$

For the other end, the same resetting is applied to the eigenmodes with a negative  $\lambda_l$ . By operating on the inverse of the left eigenmatrix ( $\mathbf{L}^{-1}$ , which is equal to  $\mathbf{R}$  if properly normalized) from the left to the characteristic equations with the modified right-hand side ( $\text{RHS}_l^*$ ), we can regain the temporal derivatives ( $\partial_t \mathbf{U}$ ) to be used to update the variables on the boundary surface. The temporal variation of the normal component of the magnetic field,  $B_i$ , is controlled in accordance with the sign of its eigenvalue,  $\lambda_l = V_i$ .

Notice that when the boundary plasma flow is outgoing and super-Alfvénic, no changes are made,  $\text{RHS}_l^* = \text{RHS}_l$ . Similarly, when the boundary plasma flow is incoming and super-Alfvénic, all temporal derivatives will be set zero,  $\text{RHS}_l^* = 0$ , hence all temporal variations should be set zero. The number of positive and negative eigenvalues on the boundary surfaces is monitored all through the simulation runs to confirm that neither of these two extreme cases had occurred in the present simulation.

## ORCID iDs

Keiji Hayashi  <https://orcid.org/0000-0001-9046-6688>  
Xueshang Feng  <https://orcid.org/0000-0001-8605-2159>  
Ming Xiong  <https://orcid.org/0000-0001-9427-7366>  
Chaowei Jiang  <https://orcid.org/0000-0002-7018-6862>

## References

- Altschuler, M. D., & Newkirk, G., Jr. 1969, *SoPh*, **9**, 131  
Aulanier, G., Torok, T., Demoulin, P., & DeLuca, E. E. 2010, *ApJ*, **708**, 314  
Bobra, M. G., Sun, X., Hoeksema, J. T., et al. 2014, *SoPh*, **289**, 3549  
Bobra, M. G., van Ballegoijen, A. A., & DeLuca, E. E. 2008, *ApJ*, **672**, 1209  
Borrero, J. M., Tomczyk, S., Kubo, M., et al. 2011, *SoPh*, **273**, 267  
Bourdin, Ph.-A., Bingert, S., & Peter, H. 2013, *A&A*, **555**, 123  
Brackbill, J. U., & Barnes, D. C. 1980, *JCoPh*, **35**, 426  
Brio, M., & Wu, C. C. 1988, *JCoPh*, **75**, 400  
Cargo, P., & Gallice, G. 1997, *JCoPh*, **136**, 446  
Centeno, R., Schou, J., Hayashi, K., et al. 2014, *SoPh*, **289**, 3531  
Cheung, M. C. M., & DeRosa, M. L. 2012, *ApJ*, **757**, 147  
Choe, J., Wang, H., Qiu, J., et al. 2001, *ApJ*, **560**, 476  
Demoulin, P., & Berger, M. A. 2003, *SoPh*, **215**, 203  
Duan, A., Jiang, C., Hu, Q., et al. 2017, *ApJ*, **842**, 119  
Fan, Y. L., Wang, H. N., He, H., & Zhu, X. S. 2011, *ApJ*, **737**, 39  
Feng, X. S., Jiang, C., Xiang, C., Zhao, X. P., & Wu, S. T. 2012, *ApJ*, **758**, 62  
Feng, X. S., Li, C., Xiang, C., et al. 2017, *ApJS*, **233**, 10  
Feng, X. S., Ma, X., & Xiang, X. 2015, *JGR*, **120**, 10159  
Fisher, G. H., Welsch, B. T., & Abbett, W. P. 2012, *SoPh*, **277**, 153  
Fisher, G. H., Welsch, B. T., Abbett, W. P., & Bercik, D. J. 2010, *ApJ*, **715**, 242  
Frutiger, C., Solanki, S. K., Fligge, M., & Bruls, J. H. M. J. 2000, *A&A*, **358**, 1109  
Galsgaard, K., Madjarska, M. S., Vanninathan, K., Huang, Z., & Presmann, M. 2015, *A&A*, **584**, A39

- Gibb, P. S., Mackay, D. H., Green, L. M., & Meyer, K. A. 2014, *ApJ*, **782**, 71
- Guo, Y., Cheng, X., & Ding, M. 2017, *SciChE*, **60**, 1408
- Guo, Y., Ding, M. D., Liu, Y., et al. 2012, *ApJ*, **760**, 47
- Harra, L. K., Archontis, V., Pedram, E., et al. 2012, *SoPh*, **278**, 47
- Harten, A. 1983, *JCoPh*, **49**, 357
- Hayashi, K. 2005, *ApJS*, **161**, 480
- Hayashi, K. 2012, *JGR*, **117**, A08105
- Hayashi, K. 2013, *JGR*, **118**, 6889
- Hayashi, K., Zhao, X. P., & Liu, Y. 2008, *JGR*, **113**, A07104
- Hoeksema, J. T., Liu, Y., Hayashi, K., et al. 2014, *SoPh*, **289**, 3483
- Hu, Q., & Dasgupta, B. 2008, *SoPh*, **247**, 87
- Inoue, S., Hayashi, K., Magara, T., Choe, G. S., & Park, Y. D. 2014, *ApJ*, **788**, 182
- Inoue, S., Shiota, D., Yamamoto, T., et al. 2012, *ApJ*, **760**, 17
- Janvier, M., Aulanier, G., & Demouline, P. 2015, *SoPh*, **290**, 3425
- Jiang, C., & Feng, X. S. 2013, *ApJ*, **769**, 144
- Jiang, C., Feng, X. S., Wu, S. T., & Hu, Q. 2013a, *ApJL*, **771**, L30
- Jiang, C., Feng, X. S., & Xiang, C. 2013b, *ApJ*, **755**, 62
- Jiang, C., Wu, S. T., Feng, X., & Hu, Q. 2014, *ApJ*, **780**, 55
- Jiang, C., Wu, S. T., Feng, X., & Hu, Q. 2016, *NatCo*, **7**, 11522
- Jing, U., Park, S.-H., Liu, C., et al. 2012, *ApJL*, **752**, L9
- Joshi, N. C., Srivastava, A. K., Filippov, B., et al. 2014, *ApJ*, **787**, 11
- Kazachenko, M. D., Fisher, G. H., Welsch, B. T., Liu, Y., & Sun, X. 2015, *ApJ*, **811**, 16
- Kazachenko, M. D., Fisher, G. H., & Welsch, T. 2014, *ApJ*, **795**, 17
- Kusano, K. 2002, *ApJ*, **571**, 532
- Kusano, K., Maeshiro, T., Yokoyama, T., & Sakurai, T. 2004, *ApJ*, **610**, 537
- Leake, J. E., Linton, M. G., & Schuck, P. W. 2017, *ApJ*, **838**, 113
- Leka, K. D., Barnes, G., Crouch, A. D., et al. 2009, *SoPh*, **260**, 83
- Leka, K. D., Canfield, R. C., & MacClymont, A. N. 1996, *ApJ*, **462**, 547
- Lemen, J. R., Title, A. M., Akin, D. J., et al. 2012, *SoPh*, **275**, 17
- Levine, R. H., & Nakagawa, Y. 1974, *ApJ*, **190**, 703
- Liu, Y. 2008, *ApJL*, **679**, L151
- Liu, Y., & Hayashi, K. 2006, *ApJ*, **640**, 1135
- Longcope, D. W. 2004, *ApJ*, **612**, 1181
- Lumme, E., Pomoell, J., & Kilpua, E. K. J. 2017, *SoPh*, **292**, 191
- Metcalf, T. R. 1994, *SoPh*, **155**, 235
- Mok, Y., Mikic, Z., Lionello, R., & Linker, J. A. 2005, *ApJ*, **621**, 1098
- Moon, Y.-J., Choe, G. S., Wang, H., et al. 2002, *ApJ*, **581**, 694
- Nagashima, K., Loptien, B., Gizon, L., et al. 2014, *SoPh*, **289**, 3457
- Nakagawa, Y., Hu, Y. Q., & Wu, S. T. 1987, *A&A*, **197**, 354
- Nakagawa, Y., & Raadu, M. A. 1972, *SoPh*, **25**, 127
- Nakagawa, Y., Raadu, M. A., Billings, D. E., & McNamara, D. 1971, *SoPh*, **19**, 72
- Nakagawa, Y., & Steinolfson, R. S. 1976, *ApJ*, **207**, 296
- Powell, K. G. 1994, ICASE Report 94-24 (Hampton, VA: NASA Langley Research Center)
- Regnier, S., & Canfield, C. 2006, *A&A*, **451**, 319
- Roe, P. L., & Balsara, D. S. 1996, *SJAM*, **56**, 57
- Sakurai, T. 1981, *SoPh*, **69**, 343
- Sakurai, T. 1982, *SoPh*, **76**, 301
- Schatten, K. H., Wilcox, J. M., & Ness, N. F. 1969, *SoPh*, **6**, 442
- Scherrer, P. H., Schou, J., Bush, R. I., Kosovichev, A. G., et al. 2012, *SoPh*, **275**, 207
- Schmidt, H. U. 1964, in *The Physics of Solar Flares*, ed. W. Hess (NASA SP-50; Washington, DC: NASA), 107
- Schou, J., Scherrer, P. H., Bush, R. I., et al. 2012, *SoPh*, **229**, 207
- Schrijver, C. J. 2016, *ApJ*, **820**, 103
- Schuck, P. W. 2006, *ApJ*, **646**, 1358
- Schuck, P. W. 2008, *ApJ*, **683**, 1134
- Shiota, D., & Kataoka, R. 2016, *SpWea*, **14**, 56
- Sun, X., Hoeksema, J. T., Liu, Y., et al. 2012, *ApJ*, **748**, 77
- Sun, X., Hoeksema, J. T., Liu, Y., Kazachenko, M., & Chen, R. 2017, *ApJ*, **839**, 67
- Tanaka, T. 1995, *JGR*, **100**, 12057
- Usmanov, A. V., Goldstein, M. L., Besser, B. P., & Fritzer, J. M. 2000, *JGR*, **105**, 12675
- Usmanov, A. V., Matthaeus, W. H., Breech, B. A., & Goldstein, M. L. 2011, *ApJ*, **727**, 84
- van Leer, B. 1979, *JCoPh*, **32**, 101
- Wang, S., Liu, C., Liu, R., et al. 2012, *ApJL*, **745**, L17
- Welsh, B. T., Abbett, W. P., DeRosa, M. L., et al. 2007, *ApJ*, **670**, 1434
- Welsh, B. T., Fisher, G. H., Abbett, W. P., & Regnier, S. 2004, *ApJ*, **610**, 1148
- Wiegmann, T., Inhester, B., & Sakurai, T. 2006, *SoPh*, **233**, 215
- Wiegmann, T., Thalmann, J. K., Inhester, B., et al. 2012, *SoPh*, **281**, 37
- Wu, S. T., Wang, A. H., Falconer, D., et al. 2012, in *ASP Conf. Ser.* 459, Numerical modeling of space plasma flows (astronom 2011), ed. N. V. Pogorelov et al. (San Francisco, CA: ASP), 254
- Wu, S. T., Wang, A. H., & Guo, W. P. 1996, *Ap&SS*, **243**, 149
- Wu, S. T., Wang, A. H., Liu, Y., & Hoeksema, J. T. 2006, *ApJ*, **652**, 800
- Wu, S. T., & Wang, J. F. 1987, *CMAME*, **64**, 267
- Yang, L. P., Feng, X. S., Xiang, C. Q., et al. 2012, *JGR*, **117**, A08110
- Yeates, A. R. 2014, *SoPh*, **289**, 631
- Yeh, T., & Dryer, M. 1985, *Ap&SS*, **117**, 165
- Zhao, J., Li, H., Parlat, E., et al. 2014, *ApJ*, **787**, 88
- Zhu, X. S., Wang, H. N., Du, Z. L., & Fan, Y. L. 2013, *ApJ*, **768**, 119